

2 **Chemical and mechanical stability of BCZY-GDC membranes for hydrogen**  
3 **separation**

4  
5 Elisa Mercadelli<sup>a</sup>, Angela Gondolini<sup>a\*</sup>, Matteo Ardit<sup>b</sup>, Giuseppe Cruciani<sup>b</sup>, Cesare Melandri<sup>a</sup>, Sonia  
6 Escolástico<sup>c</sup>, José M. Serra<sup>c</sup>, Alessandra Sanson<sup>a</sup>

7  
8 <sup>a</sup> National Council of Research, Institute of Science and Technology for Ceramics, (CNR-ISTEC),  
9 Via Granarolo 64, 48018, Faenza, Italy

10 <sup>b</sup> Department of Physics and Earth Sciences, University of Ferrara, Via Saragat 1, 44122 Ferrara,  
11 Italy

12 <sup>c</sup> Instituto de Tecnología Química (Universitat Politècnica de València-Consejo Superior de  
13 Investigaciones Científicas), Av. Los Naranjos s/n, E-46022 Valencia, Spain

14 \* Corresponding author: [angela.gondolini@istec.cnr.it](mailto:angela.gondolini@istec.cnr.it), Tel.: +39 0546699743, fax: +390546 46381

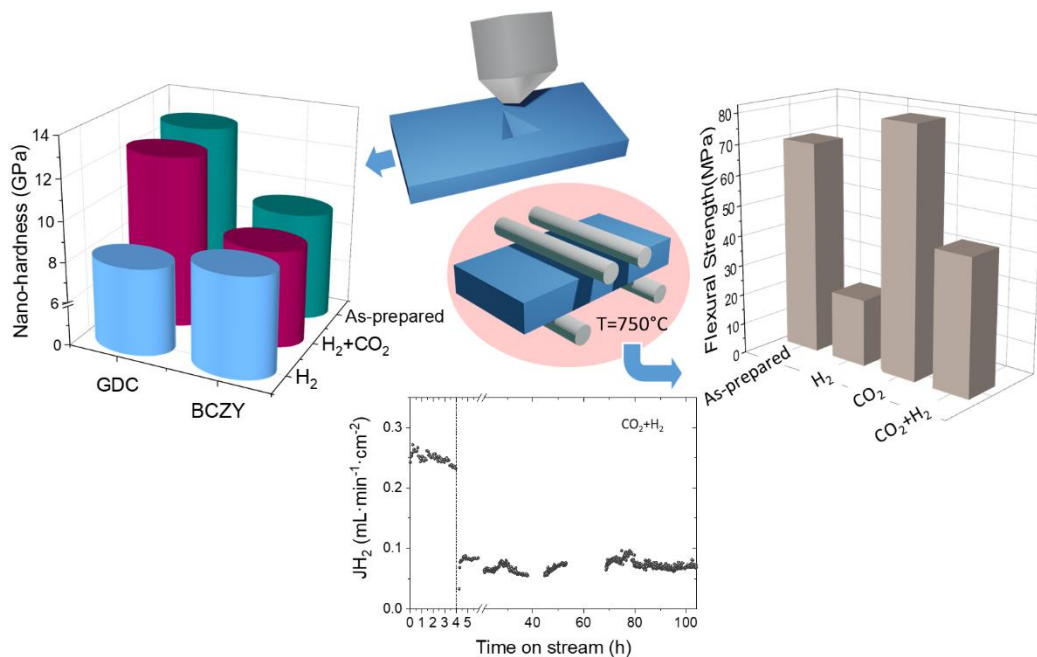
15  
16  
17 **Keywords** Ceramic composite; Hardness; Flexural strength; Aging; Operating Atmosphere

18  
19 **Abstract**

20 This work investigates, for the first time, the hydrogen permeation of  $\text{BaCe}_{0.65}\text{Zr}_{0.20}\text{Y}_{0.15}\text{O}_{3-\delta}$ -  
21  $\text{Ce}_{0.8}\text{Gd}_{0.2}\text{O}_{2-\delta}$  (BCZY-GDC) asymmetric membranes for 100 h, using wet 15%  $\text{CO}_2$  in Ar as sweep  
22 gas. In the same frame, ex-situ aging tests were performed for 100 h exposure at 750°C in different  
23 atmospheres ( $\text{H}_2$ ,  $\text{CO}_2$ ,  $\text{H}_2+\text{CO}_2$ ), to evaluate the phase, microstructure, and mechanical long-term  
24 stability of this system. The thermal aging in  $\text{H}_2$ -atmosphere leads to lower flexural strength caused  
25 by a microstructure embrittlement of the BCZY-GDC asymmetric membrane, due to chemical  
26 expansion/contraction of the GDC cell after the aging cycle. Indeed, micro-cracking of GDC grains,

27 that decreases the composite hardness, is observed in symmetric (pressed pellet) membranes. The  
 28 aging in CO<sub>2</sub> causes a slightly increase in flexural strength values due to the formation of sub-  
 29 micrometric Zr-doped ceria-BaCO<sub>3</sub> phases at the expense of the perovskite. Higher hardness values  
 30 related to the emerging of BaCO<sub>3</sub> islands on the symmetric membrane surface were also recorded.  
 31 In H<sub>2</sub>+CO<sub>2</sub> atmosphere (real testing condition), the membrane shows a slight decrease in flexural  
 32 strength and hardness while no evident morphological or structural changes (except the BaCO<sub>3</sub>  
 33 formation in traces) were observed. This study highlights that promising and stable hydrogen  
 34 permeation flux values can be recorded using the asymmetric configuration for 100 h, using wet  
 35 15% CO<sub>2</sub> in Ar as sweep gas. Neither structural nor morphological modification of the membrane  
 36 were detected after the testing.

### 37 Graphical abstract



38

### 39 1. Introduction

40 The European Commission has recently presented the new “European Green Deal”, outlining the  
 41 main policy initiatives for reaching net-zero global warming emissions by 2050 [1]. In this context,  
 42 hydrogen is confirmed to be a key instrument for meeting the Green Deal objectives, among the

43 others, i) supplying clean, affordable and secure energy, and ii) achieving a carbon neutral, clean  
44 and circular economy.

45 In this direction, the development of innovative hydrogen separation technologies, and more  
46 specifically ceramic proton-conducting membranes, is widely recognized to be an important  
47 scientific challenge to replace the conventional expensive cryogenic distillation methods in a wide  
48 range of application fields, such as fossil fuel processing, production of ammonia and metallurgy  
49 engineering, advanced chemical reactors, water-gas shift implants and methane reforming, pure H<sub>2</sub>  
50 production, etc.[2–6].

51 Mixed-conducting ceramic-ceramic composite membranes, based on the combination of a proton  
52 conducting perovskite with a suitable ceramic electron conductor, has received increasing attention  
53 [7–13] for their capability to separate hydrogen at high temperature (500-1000°C) with 100%  
54 selectivity, high chemical and thermal stability and their intrinsic lower cost respect to the Pd –  
55 based counterparts. These characteristics make Mixed Proton-Electron Conductor ceramics (MPEC)  
56 promising candidates for their easy integration into membrane reactors or pre-existent plants.

57 Among the MPEC ceramic membranes investigated so far, dense BaCe<sub>0.65</sub>Zr<sub>0.20</sub>Y<sub>0.15</sub>O<sub>3-δ</sub>-  
58 Ce<sub>0.8</sub>Gd<sub>0.2</sub>O<sub>2-δ</sub> (BCZY-GDC) composites have shown encouraging performances in terms of H<sub>2</sub>  
59 permeation, reaching H<sub>2</sub> flux values up to 0.68 mL min<sup>-1</sup> cm<sup>-2</sup> at 750 °C [14], robustness towards  
60 CO<sub>2</sub> [15] and acceptable stability under 700 ppm of H<sub>2</sub>S containing atmospheres in operating  
61 conditions [16].

62 In this regard, a lot of work has been done to assess i) the compatibility issues of the perovskite and  
63 fluorite phases during the processing steps [17], ii) the process parameters to obtain planar BCZY-  
64 GDC asymmetric membranes [18–21], iii) the structural evolution of the composite under real  
65 working conditions, i.e. high temperatures and harsh reducing conditions [22]. The latter highlights  
66 that BCZY and GDC phases show a synergic effect to reach similar volume expansion in operating

67 conditions, strengthening the real application potential of this kind of membranes. However, to  
68 effectively approach the market, the ceramic membranes must ensure long-term reliable  
69 performances under operating conditions. In this sense, the mechanical stability and phases  
70 preserving plays a crucial role in long-term operation of these systems [23]. Structural,  
71 morphological, and chemical alterations may in fact occur after long time exposure at high  
72 temperatures under operational atmospheres (that could contain CO<sub>2</sub>, CO, H<sub>2</sub>, H<sub>2</sub>O, hydrocarbons  
73 and H<sub>2</sub>S) detrimentally affecting hydrogen permeability and membrane lifespan.

74 In addition, it must be considered that the membrane thickness must be reduced as much as possible  
75 to enhance the H<sub>2</sub> permeation. A practical way is to fabricate an asymmetrical architecture in which  
76 the active membrane layer is anchored to a porous mechanically stable support [24]. Thus, the  
77 mechanical reliability of such a bi-layer composite design clearly depends on mechanical stability  
78 and the structural integrity of both the membrane and substrate.

79 Even if thermomechanical studies and lifetime predictions have been performed in deep for oxygen-  
80 conducting ceramic membranes also in asymmetrical configuration [25–27], to the best of our  
81 knowledge, very few studies have been conducted onto planar ceramic membranes for hydrogen  
82 separation, being the latter focused only onto lanthanide tungstate-based systems [28–31].

83 For BCZY-GDC-based membranes only one work has been published on the performance in CO<sub>2</sub>  
84 environment for the symmetric configuration for 24 hours of operation [15]. The hydrogen  
85 permeation rate using 15% CO<sub>2</sub> in Ar as sweep gas, 50% H<sub>2</sub> in He as the feed gas was found to be  
86 higher than 0.005 mL min<sup>-1</sup> cm<sup>-1</sup>. Due to the lack of information regarding the thermomechanical  
87 aspect, this work will present for the first time an in-depth study on the mechanical and  
88 compositional stability of these composite systems for long-term exposure in different atmosphere:  
89 (i) H<sub>2</sub>, (ii) CO<sub>2</sub> and (iii) H<sub>2</sub>+CO<sub>2</sub> mixture. The H<sub>2</sub>+CO<sub>2</sub> atmosphere was selected mimicking the one  
90 of the most common conditions used for permeation tests, i.e. 15 vol% CO<sub>2</sub> in Ar (135 mL·min<sup>-1</sup>)  
91 and H<sub>2</sub> (50 mL·min<sup>-1</sup>). The structural, microstructural and mechanical stability of BCZY-GDC after

92 100 h exposure at 750 °C in the different abovementioned atmospheres was accurately investigated  
93 to highlight the effect of each atmosphere on phase composition, microstructure and mechanical  
94 properties. Finally, hydrogen permeation of BCZY-GDC asymmetric membrane was evaluated, for  
95 the first time, in 100 h of operation, using wet 15% CO<sub>2</sub> in Ar as sweep gas to assess its long-term  
96 performances. Structural stability was studied by X-ray diffraction and TG measurements whereas  
97 microstructural properties were studied by SEM. Mechanical properties of the composite before and  
98 after the treatments were characterized by three different techniques: 4-pt flexure strength at 750 °C,  
99 indentation and nano-indentation at room temperature. To the author best knowledge this is the first  
100 time that the mechanical properties of BCZY- GDC systems were investigated in real atmosphere  
101 and temperature of operation. This work will represent therefore a huge step forward the  
102 understanding of the structural, microstructural and mechanical behavior of BCZY-based ceramic  
103 membrane in real conditions.

104

## 105 **2. Experimental**

### 106 2.1 Membranes production

107 BCZY-GDC composite membranes were produced both in asymmetrical and symmetrical  
108 configuration as required for each specific characterization/testing technique implemented in this  
109 work.

110 The asymmetric BCZY-GDC membranes were prepared by tape casting. For the porous support,  
111 BCZY (BaCe<sub>0.65</sub>Zr<sub>0.20</sub>Y<sub>0.15</sub>O<sub>3-δ</sub>, Specific Surface Area (SSA) = 5.8 m<sup>2</sup>/g, supplied by Marion  
112 Technology, France) and GDC powders (Ce<sub>0.8</sub>Gd<sub>0.2</sub>O<sub>2-δ</sub>, SSA = 6.8 m<sup>2</sup>/g, supplied by  
113 FuelCellMaterials, USA) were used as starting material in a ratio equal to 50/50 vol %. Rice Starch  
114 (Fluka, Germany), with average particle size of 5-6 μm was used as sacrificial pore forming agent.  
115 The amount of starch added to the slurry was the 53 vol % respect to the ceramic powder as

116 previously optimized in [20]. On the other hand, BCZY (SSA = 12.2 m<sup>2</sup>/g, supplied by Marion  
117 Technology, France) and GDC powders in a ratio equal to 50/50 vol % were used to produce the  
118 dense membrane layer. An amount of 1 wt% ZnO (Sigma Aldrich) respect to the powders was used  
119 as sintering aid and directly added into the tape casting suspension. For a detailed description of the  
120 slurry's composition, preparation and casting parameters, the interested reader is referred to the  
121 previous works [18,20].

122 The green tapes were punched in discs of 24 mm in diameter for the permeation test, while for  
123 bending tests, strips of 35 x 8 mm<sup>2</sup> size were cut. An uniaxial warm press (55 °C applying a  
124 pressure of 0.7 bar) was used to laminate the porous support with the active membrane layer to  
125 produce the asymmetrical BCZY-GDC structure.

126 The bilayers were finally debinded and sintered at 1550 °C for 4 h. A 50/50 vol% mixture of  
127 BCZY-GDC was used as source of barium during sintering following the experimental set-up  
128 already reported in [19]. The resulting asymmetric membranes were 0.65 ± 0.5 mm thick.

129 The symmetric BCZY-GDC membranes were prepared by die pressing. The 50/50 vol% mixture of  
130 BCZY-GDC powders with 1 wt % ZnO was ball milled in ethanol (99 %, Sigma Aldrich) for 2 h,  
131 dried at 50 °C and finally sieved at 75 µm. The resulting powder was uniaxially pressed in a Ø = 12  
132 mm die at 750 Kg/cm<sup>2</sup> and isostatically pressed at 3000 bar. The green pellets were finally sintered  
133 at 1550 °C for 4 h, with the same sintering set-up used for the tape cast membranes. All the sintered  
134 pellets reached relative density values of 98.4 ± 0.8 %.

## 135 2.2 Aging treatments

136 To investigate the influence of the operating atmosphere on the thermomechanical stability of the  
137 BCZY-GDC membranes, both symmetrical and asymmetrical membranes were aged at 750°C for  
138 100h in different atmospheres: H<sub>2</sub>, CO<sub>2</sub> and H<sub>2</sub>+CO<sub>2</sub>. In the case of symmetrical membranes, one  
139 surface side of each pellet was polished down to 0.25 µm finish before the aging treatment to

140 perform the nano-indentation tests. All the samples were placed onto ad-hoc perforated alumina  
141 setters (Keralpor 99, Kerafol) to guarantee the maximum exposure to the aging atmosphere.

142 The aging treatment in reducing atmosphere was performed in a tubular furnace (Nabertherm,  
143 Germany), setting an Ar/H<sub>2</sub> (4 vol%) flow rate equal to 50 L h<sup>-1</sup>. On the other hand, samples were  
144 aged in a saturated CO<sub>2</sub> atmosphere in a conventional furnace setting a pure CO<sub>2</sub> flow equal to 50 L  
145 h<sup>-1</sup>. The third aging treatment was performed in a tubular reactor under a stream composed by 15  
146 vol% CO<sub>2</sub> in Ar (135 mL·min<sup>-1</sup>) and H<sub>2</sub> (50 mL·min<sup>-1</sup>). This gas composition was selected to be  
147 comparable with the one used during the permeation test (same gas flows).

### 148 2.3 Characterizations

149 The 4-pt flexural strength of the as-prepared and thermally aged asymmetric membranes was  
150 measured at 750 °C in Ar flow (3.5 L min<sup>-1</sup>) using the furnace HTTF 974 (Severn Furnaces). The  
151 tape cast bars with dimensions about 25.5 × 5.5 × 0.6 mm<sup>3</sup> (length by width by thickness,  
152 respectively) were tested using a universal screw-driven load frame for mechanical testing (Instron  
153 mod. 1195, Instron). An alumina flexural jig with upper and lower span of 10 and 20 mm,  
154 respectively was used, while the specimens were broken with a crosshead speed of 0.5 mm min<sup>-1</sup>.  
155 Before applying the load during testing at high temperature, a dwell of 15 min was set to reach  
156 thermal equilibrium. For each set of samples, at least 5 bars were tested.

157 Vickers microhardness (HV) was measured on the polished surface of the as-prepared and  
158 thermally aged symmetric BCZY-GDC membranes (pellets), with a load of 4.9 N, using a  
159 Innovatest Falcon 505 (Innovatest, The Netherlands) indenter. The value provided (expressed in  
160 HV) is the average of 10 indentations.

161 Nano-hardness of BCZY and GDC grains was investigated using a commercial nanoindenter (MTS  
162 mod. XP, MTS Systems Corporation, Oak Ridge, TN, USA) equipped with a Berkovich diamond  
163 tip. The tests were performed using polished samples (as prepared and thermally aged BCZY-GDC

164 composite pellets) with a peak load of 5 mN. The nano-indenter was continuously loaded with a  
165 strain rate target of  $0.05 \text{ s}^{-1}$  up to the peak load and immediately unloaded with no holding time. For  
166 each sample 90 indentations, spaced at  $5 \mu\text{m}$ , were made. Hardness (H) was calculated according to  
167 a computational procedure included in the nanoindenter software TestWorks™ ver. 4.06 A, which  
168 is based on the model of Oliver and Pharr (2004). The software automatically subtracted both the  
169 machine compliance and thermal drift. The nano-hardness values are expressed in GPa.

170 Prior to X-Ray Powder Diffraction (XRPD) analyses, as-prepared and thermally aged asymmetric  
171 membranes were ground in an agate mortar with a pestle. Data collection was performed at room-  
172 temperature (RT) on a Bruker D8 Advance Da Vinci diffractometer working in Bragg-Brentano  
173 geometry, and equipped with a Cu-anode X-ray tube, Ni-filter to suppress Cu  $K\beta$  component, and a  
174 LynxEye XE silicon strip detector (angular range of the detector window size =  $2.585^\circ 2\theta$ ) set to  
175 discriminate Cu  $K\alpha_{1,2}$  radiation. The powder of each sample was placed over a monocrystalline Si  
176 low background sample holder and scanned in a continuous mode from  $5\text{-}135^\circ 2\theta$  with step size of  
177  $0.015^\circ 2\theta$  and a counting time of 1.5 s per step. To minimize the preferred orientation of  
178 crystallites, the sample was spun at 25 rpm to increase crystallite statistics, and a knife  
179 perpendicular to the sample was placed at a suitable distance from the sample surface to reduce the  
180 air-induced scattering. An additional measurement at RT was performed using the same  
181 experimental setup on the bulk BCZY-GDC membrane on both dense and porous side after  
182 permeation tests.

183 Qualitative phase analysis was performed by means of the Bruker AXS EVA software (v.5), while  
184 each collected X-ray powder diffraction pattern was Rietveld refined by means of the fundamental-  
185 parameter approach (TOPAS v.5.0). All the identified phases were modeled by carrying out  
186 multiphase refinements in which only the scale factor, unit-cell parameters, and the crystallite size  
187 were varied. The crystallite size was calculated by means of the "integral breadth" based LVol  
188 calculation derived from a profile peak convolution in a Lorentzian-type broadening approximation.



189 Results of the quantitative phases analysis for the bulk BCZY-GDC membrane after permeation  
190 tests (Table S1) are deposited as supplemental material.

191 Thermogravimetric (TG) analysis (STA 449, Netzsch, Selb/Bavaria, Germany) was performed to  
192 assess the CO<sub>2</sub> uptake of the asymmetric BCZY-GDC membrane at 750 °C for 100 h. 80 mL min<sup>-1</sup>  
193 of dry CO<sub>2</sub> and 20 mL min<sup>-1</sup> of dry N<sub>2</sub> were fed during the analysis.

194 The microstructure of the sintered membranes was investigated by scanning electron microscopy  
195 (SEM-FEG, Carl Zeiss Sigma NTS GmbH, Oberkochen, Germany), embedding the cross sections  
196 under vacuum in epoxy resin and then polishing them down to 0.25 μm finish. For the asymmetrical  
197 membranes, the porosity amount of the support as well as the residual porosity and thickness of the  
198 dense active layer were calculated via image analysis of the SEM micrographs using ImageJ  
199 software (Java, ORACLE, Redwood City, California). The chemical composition before and after  
200 the aging treatment was assessed by semi-quantitative analysis with an EDS probe (EDS, X-Act,  
201 INCA Energy 300, Oxford Instruments, Abingdon, UK).

202 Hydrogen permeation stability of the as-prepared asymmetric BCZY-GDC membrane was  
203 evaluated for 100 h by using as sweep side an atmosphere composed by 15 vol% CO<sub>2</sub> in Ar (135  
204 mL·min<sup>-1</sup>) at 750 °C. A mixture of 1:1 H<sub>2</sub>-He (100 mL·min<sup>-1</sup>) was used as feed gas. Both streams  
205 were humidified at room temperature (3 % H<sub>2</sub>O). Sweep gas was fed on the porous substrate  
206 whereas feed gas was introduced on the dense membrane layer. The H<sub>2</sub> content in the permeate side  
207 was analyzed using micro-GC Varian CP-4900 equipped with Molsieve5A and PoraPlot-Q glass  
208 capillary modules. Sealing was accomplished using a silver-based alloy ring.

209 The surface of the dense membrane and the porous support were catalytically activated with Pt. A  
210 Pt catalytic layer was screen-printed on the dense membrane side whereas the porous support was  
211 infiltrated with a 0.15 M solution of Pt (tetraammineplatinum (II) nitrate). Subsequently, sample  
212 was dried at 150 °C and calcined at 750 °C.

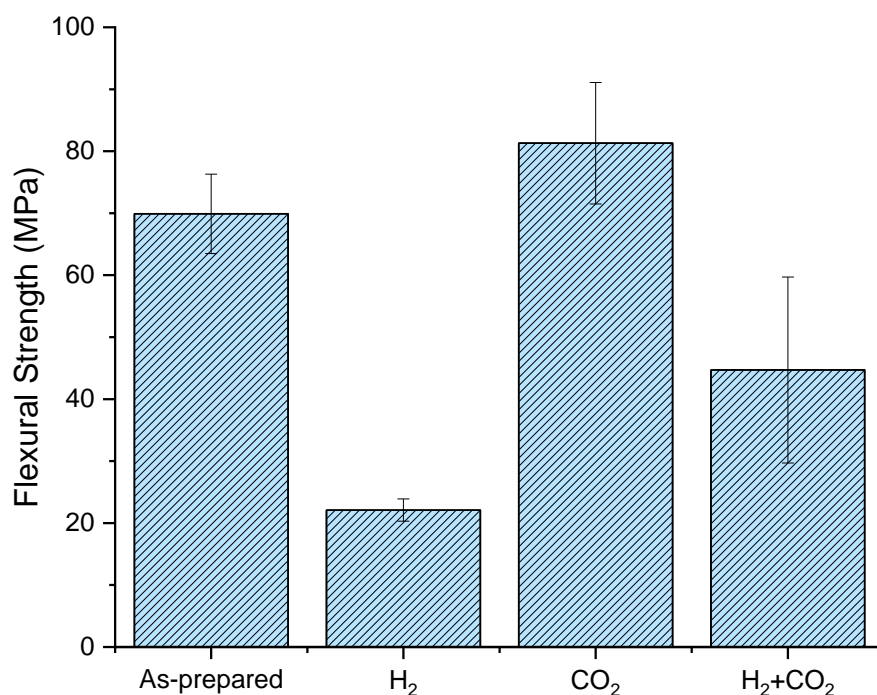
213

### 214 3. Results and Discussion

#### 215 3.1 Flexural tests of asymmetric BCZY-GDC membranes

216 The influence of the aging atmosphere on the thermomechanical stability of the asymmetric BCZY-  
217 GDC membranes was investigated through 4-pt flexure tests at the selected working temperature of  
218 750°C. The results are illustrated in Figure 1.

219 Collected data show that the flexural strength values are in the same order of magnitude of dense  
220 (symmetrical) lanthanum tungstate-based membranes tested at high temperatures [30], i.e., around  
221 70 MPa for untreated samples. The nature of the aging atmosphere strongly influences the  
222 mechanical performances of the present membranes as can be observed in Figure 1. In particular,  
223 the membranes exposed to H<sub>2</sub> atmosphere registers a collapse of the flexural strength values while  
224 the membranes aged in CO<sub>2</sub> show a slightly higher flexural strength compared to the ones collected  
225 for the as-prepared samples. Lastly, the thermal treatment in H<sub>2</sub>+CO<sub>2</sub> atmosphere leads to strength  
226 values that are in between to those registered for the two single atmospheres (H<sub>2</sub> and CO<sub>2</sub>). This  
227 result indicates that for the asymmetric membrane there is a balancing effect between the increase  
228 of the flexural strength due to the CO<sub>2</sub> treatment and the embrittlement of the structure given by H<sub>2</sub>.



229

230 **Figure 1** Flexural strength values of asymmetric BCZY-GDC membranes registered at 750°C after  
 231 thermal aging at 750°C for 100 h in different atmospheres: as-prepared, H<sub>2</sub>, CO<sub>2</sub> and H<sub>2</sub>+CO<sub>2</sub>.

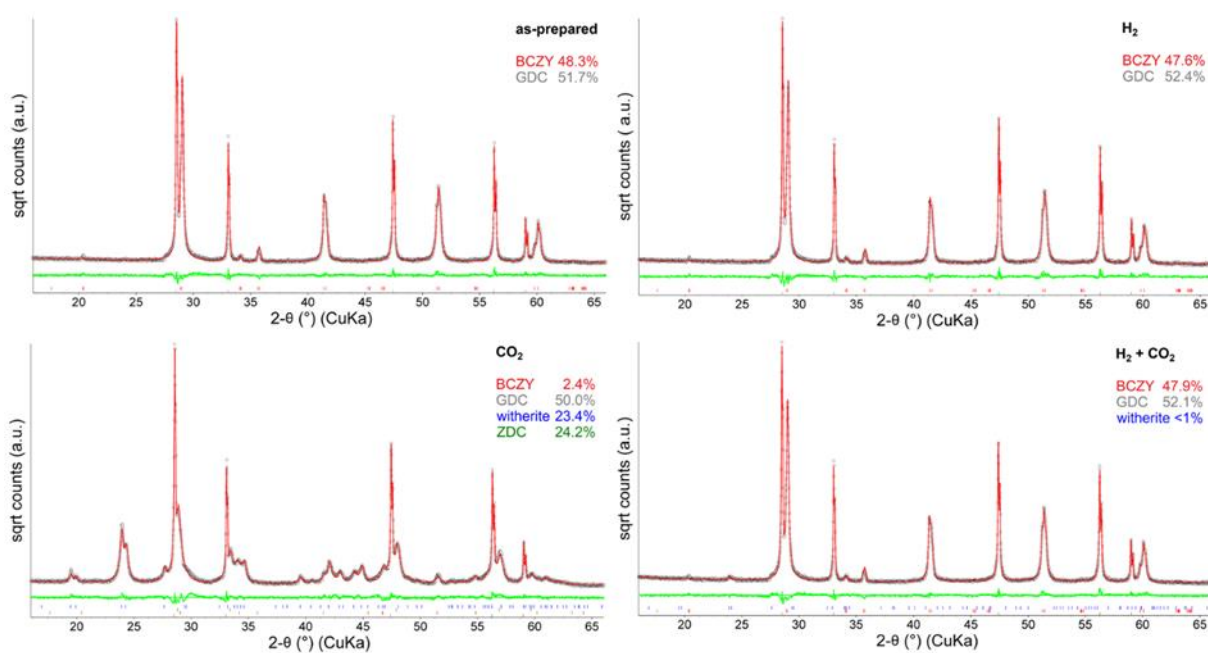
232

### 233 3.2 Microstructural and morphological characterization of asymmetric membranes

234 To understand the as-described mechanical behaviour, the influence of the operating atmosphere on  
 235 the microstructural and morphological properties of the asymmetric BCZY-GDC membranes were  
 236 investigated through XRD and SEM-EDS analyses.

237 Rietveld refinement plots for collected XRPD patterns of the as-prepared and aged membranes are  
 238 reported in Figure 2, while the results of the quantitative phases analysis are shown in Table 1 and  
 239 as in-set graphs inside the corresponding plot. Refinement of the as-prepared BCZY-GDC  
 240 membrane confirms the presence of both GDC and BCZY phases with phase fractions equal to 51.7  
 241 ± 0.1 % GDC and 48.3 ± 0.1 % BCZY in weight. The resulting phase fraction is very closed to the

242 nominal one, where a 50-50 vol.% corresponding to 54-46 wt% GDC-BCZY phase proportion is  
243 expected, thus confirming that the constituting phases are preserved during the production process.  
244 The phase fraction ratio of perovskite- and fluorite-type crystal structures is also maintained when  
245 the membrane is exposed for 100 h at 750°C in H<sub>2</sub> and H<sub>2</sub>+CO<sub>2</sub> atmosphere (Table 1), although in  
246 the latter condition the partial reaction between the BCZY and CO<sub>2</sub> leads to the formation of  
247 detectable traces of witherite BaCO<sub>3</sub> (< LoQ value). Nevertheless, a remarkable compositional  
248 variation is detected when the asymmetric membrane is aged in pure CO<sub>2</sub> atmosphere. Unlike the  
249 GDC fluorite phase, which is not affected by thermal aging treatments, the BCZY perovskite tends  
250 to completely decompose under CO<sub>2</sub> atmosphere (2.4 wt% of residual perovskite is detected) in  
251 favour of an almost equal amount of witherite BaCO<sub>3</sub> (23.4 wt%) and Zr-doped ceria ZDC (24.2  
252 wt%). The chemical stability against the CO<sub>2</sub> of BCZY-based compounds is in fact a well-known  
253 critical issue [32].



254  
255 **Figure 2** Rietveld refinement plots of the XRPD patterns collected at RT for investigated  
256 asymmetric BCZY-GDC membranes (i.e. as prepared and aged at 750 °C for 100 h in different  
257 atmospheres). The experimental profile is represented by black dots, the continuous red line is the

258 calculated pattern, while the lower grey curve is the difference between calculated and observed  
 259 intensities. Vertical ticks mark the position of phase reflections.

260

261 **Table 1.** Refinement agreement factors, quantitative phase analysis, unit-cell parameters, and  
 262 crystallite size with their standard deviations for the BCZY-GDC as-prepared membrane and after  
 263 treatments at 750 °C for 100 h in different aging atmospheres (*i.e.*, H<sub>2</sub>, CO<sub>2</sub>, and H<sub>2</sub>+CO<sub>2</sub>). BCZY,  
 264 GDC, and ZDC stand for Ba(Ce<sub>0.65</sub>Zr<sub>0.2</sub>Y<sub>0.15</sub>)O<sub>2.925</sub> with perovskite structure and, (Ce<sub>0.8</sub>Gd<sub>0.2</sub>)O<sub>1.9</sub>  
 265 and (Ce<sub>1-x</sub>Zr<sub>x</sub>)O<sub>2</sub> (ZDC) with fluorite-type structure, respectively.

	Phase	R <sub>Bragg</sub>	Wt%	s.g.	<i>a</i> (Å)	<i>b</i> (Å)	<i>c</i> (Å)	<i>V</i> (Å <sup>3</sup> )	Crystallite size (nm)	R <sub>wp</sub>
As- prepared	BCZY	0.043	48.3(1)	<i>Imma</i>	6.1538(2)	8.6861(2)	6.1819(1)	330.43(1)	198(10)	0.085
	GDC	0.040	51.7(1)	<i>Fm-3m</i>	5.4206(2)	–	–	159.27(1)	225(11)	
H <sub>2</sub>	BCZY	0.049	47.6(1)	<i>Imma</i>	6.1538(2)	8.6848(2)	6.1816(1)	330.38(1)	243(19)	0.096
	GDC	0.040	52.4(1)	<i>Fm-3m</i>	5.4209(2)	–	–	159.30(1)	220(15)	
CO <sub>2</sub>	BCZY	0.016	2.4(1)	<i>Imma</i>	–	–	–	–	32(7)	0.092
	GDC	0.039	50.0(3)	<i>Fm-3m</i>	5.4201(2)	–	–	159.22(1)	215(5)	
	witherite	0.029	23.4(2)	<i>Pmcn</i>	5.3053(4)	8.9109(6)	6.4490(5)	304.87(4)	32(7)	
	ZDC	0.039	24.2(5)	<i>Fm-3m</i>	5.3647(1)	–	–	154.40(1)	32(7)	
H <sub>2</sub> +CO <sub>2</sub>	BCZY	0.052	47.9(1)	<i>Imma</i>	6.1543(2)	8.6863(2)	6.1813(1)	330.44(1)	148(6)	0.086
	GDC	0.043	52.1(1)	<i>Fm-3m</i>	5.4204(2)	–	–	159.25(1)	216(9)	
	witherite	–	< 1.	<i>Pmcn</i>	–	–	–	–	–	

266 NOTE: since the formation of witherite and ZDC phases takes place at the expenses of the BCZY phase, the  
 267 crystallite size for those phases has been constrained to be the same.

268

269 The BaCO<sub>3</sub> formation, resulting from X-ray diffraction analysis, is corroborated by the data  
 270 registered as weight variation for the asymmetric membranes before and after the aging treatment in  
 271 CO<sub>2</sub> and H<sub>2</sub>+CO<sub>2</sub> atmosphere (Table 2). Furthermore, the thermogravimetric curve (Figure 3)  
 272 registered for the asymmetric membrane under a CO<sub>2</sub>-N<sub>2</sub> flux (80 vol% of CO<sub>2</sub>) suggests similar  
 273 values of CO<sub>2</sub> uptake, highlighting the highest rate of carbonation reaction after 1000 min (16 h) at  
 274 750°C, reaching a weight stabilization after 5000 min (83 h).

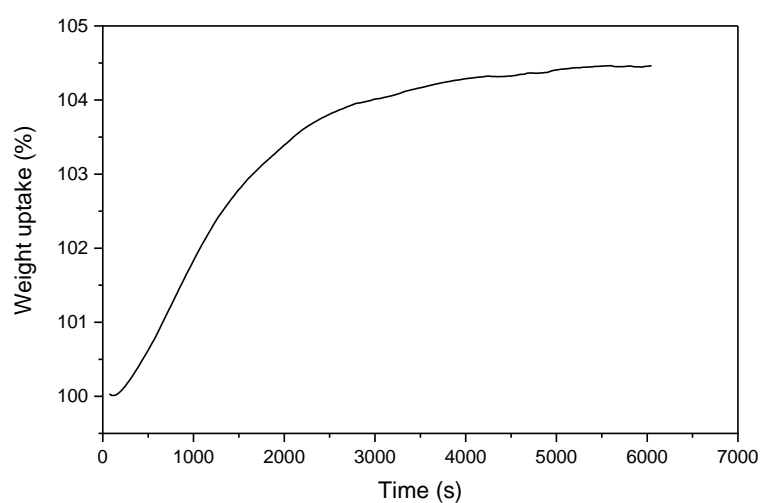
275

276

**Table 2** Weight variation registered for the asymmetric BCZY-GDC membranes.

<b>Aging atmosphere</b>	<b>CO<sub>2</sub> uptake (wt%)</b>	<b>BaCO<sub>3</sub> (wt%)</b>
CO <sub>2</sub>	5.3 ± 0.1	23.9 ± 0.6
H <sub>2</sub> +CO <sub>2</sub>	0.09 ± 0.04	0.4 ± 0.2

277



278

**Figure 3** Thermogravimetric curve registered at 750 °C for an asymmetric BCZY-GDC membrane under CO<sub>2</sub> (80 mL min<sup>-1</sup>) - N<sub>2</sub> (20 mL min<sup>-1</sup>) flux.

281

282 Further evidence on the effects of thermal aging treatments undergone by the BCZY-GDC  
 283 membranes can be inferred from the variation of unit-cell parameters and crystallite size of detected  
 284 phases (Table 1). While the GDC phase is unaffected from treatments in different atmospheres (i.e.  
 285 lattice parameters vary within uncertainties, and the same crystallite size is retained), the BCZY  
 286 with perovskite structure seems to be more reactive at the different external conditions. The latter  
 287 phase, that keeps almost unchanged after the treatment in H<sub>2</sub>, shows a first evidence of phase  
 288 transformation after the aging in H<sub>2</sub>+CO<sub>2</sub> atmosphere. Although volumetric changes are not

289 observed, a 25% crystallite size decreasing (i.e. from ~200 nm of the as-prepared sample to ~150  
290 nm) occurred. Nevertheless, as previously observed, the prolonged aging in CO<sub>2</sub> atmosphere  
291 promotes the formation of witherite and Zr-doped ceria at BCZY perovskite expense. The new  
292 phases as well as the residual BCZY are characterized by a crystallite size which is one seventh (i.e.  
293 about 30 nm) of that of the BCZY perovskite phase in the as-prepared membrane. The formation of  
294 these sub-micrometric Zr-doped ceria-BaCO<sub>3</sub> phases at the expense of the perovskite, strengthening  
295 the membrane microstructure due to the toughening mechanism of the matrix by sub-micrometric  
296 particles [33–35] (Figure 1).

297 Summarizing, the data collected from X-ray analysis performed onto asymmetric membranes  
298 suggest that: i) the BCZY phase tends to completely reacts with CO<sub>2</sub> at 750 °C, in saturated CO<sub>2</sub>  
299 atmosphere, forming BaCO<sub>3</sub> and Zr-doped ceria phases constituted by nanometric-size crystals; ii)  
300 no remarkable evidence of changes onto membranes aged in H<sub>2</sub>; iii) the aging treatment in H<sub>2</sub>+CO<sub>2</sub>  
301 atmosphere leads to the formation of < 1 wt% BaCO<sub>3</sub> after 100 h, and to a BCZY crystallite size  
302 decrease of about 25%.

303 To further investigate the effect of the operating atmosphere onto the morphological properties of  
304 the asymmetric membranes, SEM-EDS analyses were performed before and after each aging  
305 treatment. The micrographs of the polished cross sections of the asymmetric membranes aged at  
306 750°C for 100 h in H<sub>2</sub>, CO<sub>2</sub> or H<sub>2</sub>+CO<sub>2</sub> are reported in Figure 4. The as-prepared membrane is  
307 constituted by a highly porous (44 ± 2%) support and a 16 ± 1 μm thick active layer with closed  
308 porosity < 5 % (Figure 4a). Moreover, SEM analysis of the backscattered electron (BSE) evidences  
309 a homogeneous distribution of light grey areas related to the GDC phase as well as dark areas  
310 attributed to BCZY. The peculiar topography of the polished cross sections shown in Figure 5 is the  
311 result of the hardness contrast between the harder GDC (light grey) and the softer BCZY (dark) as  
312 already observed in [14].

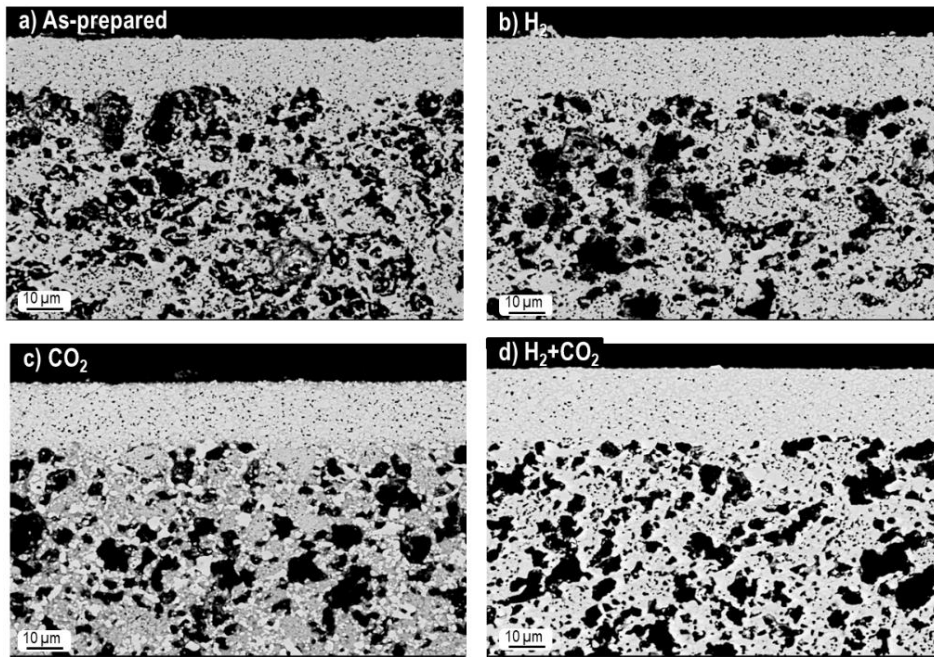
313 When the membrane is aged in H<sub>2</sub> atmosphere (Figure 4b), no apparent morphological differences  
314 can be observed. However, some cracks across the active membrane layer were detected after  
315 sample embedding/polishing. This indicates that structural changes occur in the membrane during  
316 the thermal cycle under H<sub>2</sub> at 750 °C for 100 h and back to ambient (oxidant) atmosphere,  
317 favouring the embrittlement of the membrane and thus lowering its fracture strength. In fact, even if  
318 no cell parameters variation was registered after this aging treatment due to re-oxidation phenomena  
319 in ambient atmosphere (Table 1), it is widely demonstrated from in-situ synchrotron XRD analyses  
320 in reducing conditions [22,36] that doped-CeO<sub>2</sub> materials show a significant non-linear expansion  
321 of the cubic cell due to the reduction of Ce<sup>4+</sup> to Ce<sup>3+</sup>, predominant at T > 600°C.

322 On the other hand, a morphological transformation was clearly detected for the sample aged in CO<sub>2</sub>  
323 (Figure S1). The dark grey areas related to BCZY are in fact replaced by sub-micrometric grains  
324 (either dark or light), mainly distinguishable on the top surface of the dense active layer and  
325 throughout the porous support section. This phenomenon is reasonably associated to the  
326 decomposition of the perovskite phase into BaCO<sub>3</sub> (dark grains) and ZDC (light grains) as  
327 previously demonstrated by XRD analyses.

328 Finally, no morphological changes can be appreciated when the membrane is subjected to a thermal  
329 cycle at 750 °C for 100 h in H<sub>2</sub>+CO<sub>2</sub> atmosphere (Figure 4d).

330 Focused electron beam EDS profiles of Ba, Gd and C elements (Figure S2) were also recorded on  
331 the polished fractures of the active membrane layer to assess the stability towards CO<sub>2</sub> and to  
332 confirm the distribution of BCZY and GDC. EDS profiles for Ba and Gd demonstrate the  
333 homogeneous distribution of the fluorite and perovskite phases for the membranes investigated. On  
334 the other hand, EDS profile of carbon confirms the lack of carbonated species in the as-prepared,  
335 H<sub>2</sub>- and H<sub>2</sub>+CO<sub>2</sub>-aged samples, while a detectable carbon concentration profile is visible for the  
336 membrane aged in CO<sub>2</sub>, especially in the first 1.0 μm starting from the upper surface.





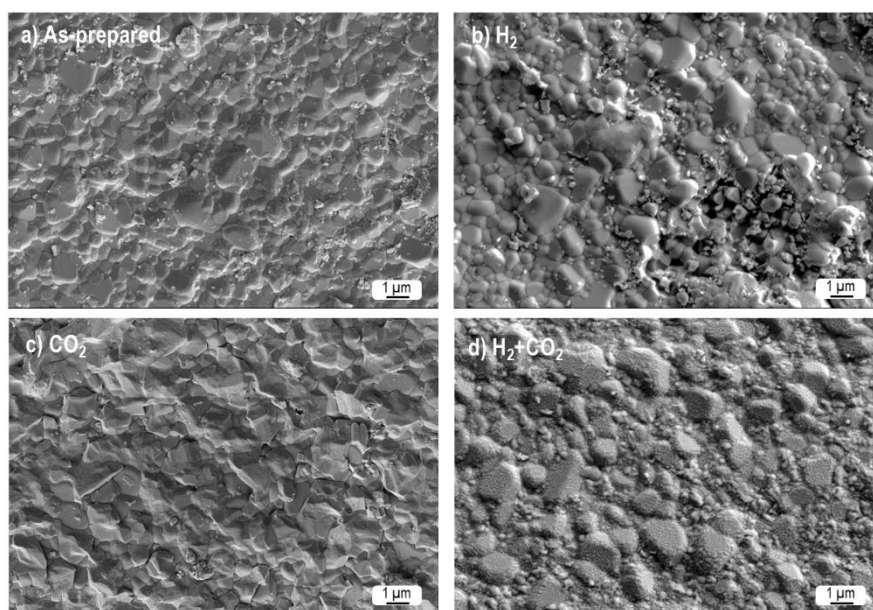
337

338 **Figure 4** BSE-SEM micrographs of the polished cross sections of the asymmetric membranes aged  
 339 at 750 °C for 100 h in different atmospheres: as-prepared (a), H<sub>2</sub> (b), CO<sub>2</sub> (c), H<sub>2</sub>+CO<sub>2</sub> (d).

340

341 Finally, the influence of the aging treatment at 750°C for 100 h in different atmospheres on the  
 342 dense active layer surface morphology of the asymmetric membranes is shown in Figure 5.  
 343 According to the previously reported results, no detectable surface modification is registered for the  
 344 membrane treated in H<sub>2</sub> atmosphere that show the same round-shape grains microstructure. On the  
 345 other hand, morphological alterations occur when the membranes are aged in H<sub>2</sub>+CO<sub>2</sub> and CO<sub>2</sub>  
 346 atmospheres. Even if the former preserves the grain boundary microstructure (with respect to as-  
 347 prepared sample), small amounts of impurity phase (i.e. BaCO<sub>3</sub>, in accordance with the Rietveld  
 348 refinement results) in the nanometric range are clearly distinguished at the grains surface. A similar  
 349 surface modification has been already observed for BCZY-based ceramic pellets after CO<sub>2</sub> exposure  
 350 at 700 °C for 10 h [37]. Indeed Cheng et al. showed a similar surface microstructure for a  
 351 BaCe<sub>0.8</sub>Y<sub>0.2</sub>O<sub>3-δ</sub>-Ce<sub>0.8</sub>Y<sub>0.2</sub>O<sub>2-δ</sub>/BaCe<sub>0.8</sub>Y<sub>0.2</sub>O<sub>3-δ</sub>-Ni hollow fiber membrane after stability test at 850  
 352 °C (125 h), using 7% CO<sub>2</sub>-N<sub>2</sub> as the sweep gas, even if no discussion was given about the nano-

353 sized impurities formation localized at the membrane surface [38]. On the contrary, a significant  
354 change in the microstructure of the BCZY-GDC dense surface after CO<sub>2</sub> treatment (Figure 5c) is  
355 observed due to the presence of sharp-cornered grains microstructure in respect to the ones reported  
356 in Figure 5 a) and b). The grains of this microstructure are present continuously on the upper  
357 surface of the CO<sub>2</sub> aged membrane and they are attributed to a witherite coating formed by the CO<sub>2</sub>-  
358 BCZY reaction.



359  
360 **Figure 5** SEM micrographs of the dense active layer surface of the asymmetric membranes aged at  
361 750 °C for 100 h in different atmospheres: as-prepared (a), H<sub>2</sub> (b), CO<sub>2</sub> (c), H<sub>2</sub>+CO<sub>2</sub> (d).

362 Thereby, according to the XRD data coupled with SEM results, the mechanical behaviour of  
363 asymmetric BCZY-GDC membranes can be explained as follow: i) the exposure of the membrane  
364 to H<sub>2</sub>-atmosphere (at 750°C x 100 h) leads to a lower flexural strength caused by a general  
365 embrittlement of the structure probably consequence of chemical expansion/contraction of the GDC  
366 cell after the aging cycle; it has been already noticed [39,40] that the reduction of Ce<sup>4+</sup> to Ce<sup>3+</sup>  
367 provokes an expansion of lattice resulting in mechanical strains that could affect the lifespan of this  
368 material; ii) the aging in CO<sub>2</sub> atmosphere causes an increase in flexural strength values due to the  
369 formation, especially in the porous support, of ZDC-BaCO<sub>3</sub> sub-micrometric phases at the expense

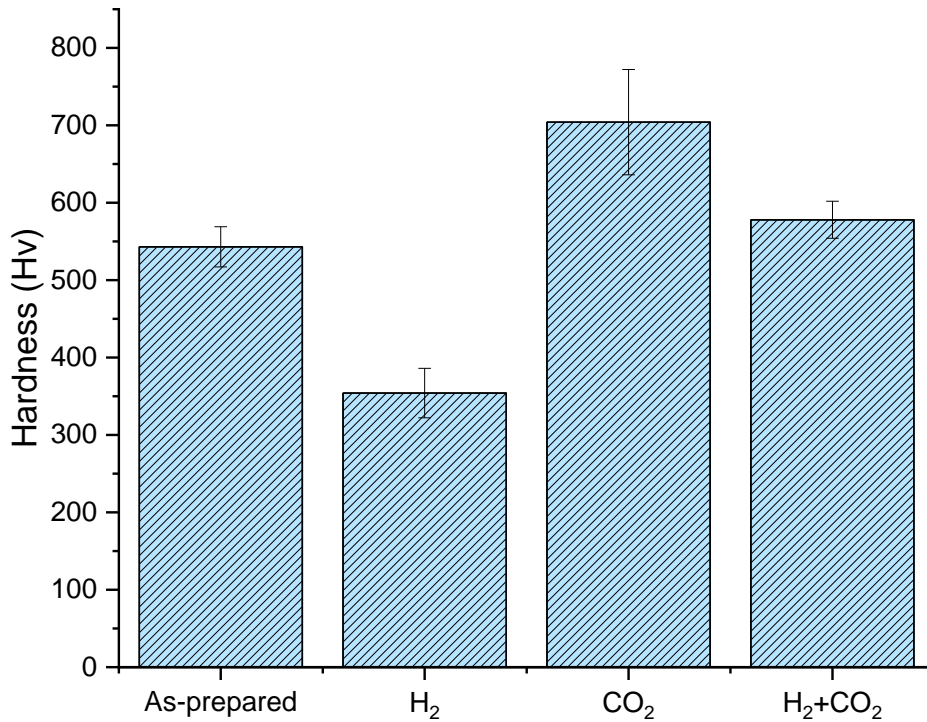
370 of the perovskite, strengthening the membrane microstructure; iii) the membrane aged in the  
371 operating  $H_2+CO_2$  atmosphere, simulating the one used during practical permeation test, shows  
372 only a slight decrease in flexural strength because no evident morphological or structural changes  
373 (except the  $BaCO_3$  formation in trace amount) were observed.

374

375 3.3 Indentation/nano-indentation tests of symmetric BCZY-GDC membranes and their  
376 morphological characterization

377 To further investigate the mechanical behaviour of BCZY-GDC composite, indentation and  
378 nanoindentation tests were performed onto symmetric membranes (pressed pellets) before and after  
379 the same aging treatments used for their corresponding asymmetric structures.

380 The hardness values reported in Figure 6 show a trend comparable to the one registered for the  
381 flexural strength of the asymmetric membranes (Figure 1) apart from the values registered in  
382  $H_2+CO_2$  atmosphere. Similarly, while a thermal aging in  $H_2$  atmosphere causes a hardness decrease,  
383 the exposure to  $CO_2$  leads to hardness increase. On the other hand, hardness values of symmetric  
384 membrane aged in  $H_2+CO_2$  atmosphere remain almost constant indicating a negligible influence of  
385 the  $H_2+CO_2$  atmosphere on the hardness values. This result, apparently in contrast with the trend  
386 observed for flexural strength (Figure 1), is nonetheless roughly a balance between the values  
387 registered after aging in  $H_2$  and  $CO_2$  as observed for the flexural strengths of the asymmetric  
388 structures.



389

390 **Figure 6** Hardness values measured by indentation tests of symmetric BCZY-GDC membranes  
 391 (pellets) registered after thermal aging at 750 °C for 100 h in different atmospheres (as-prepared,  
 392 H<sub>2</sub>, CO<sub>2</sub> and H<sub>2</sub>+CO<sub>2</sub>).

393

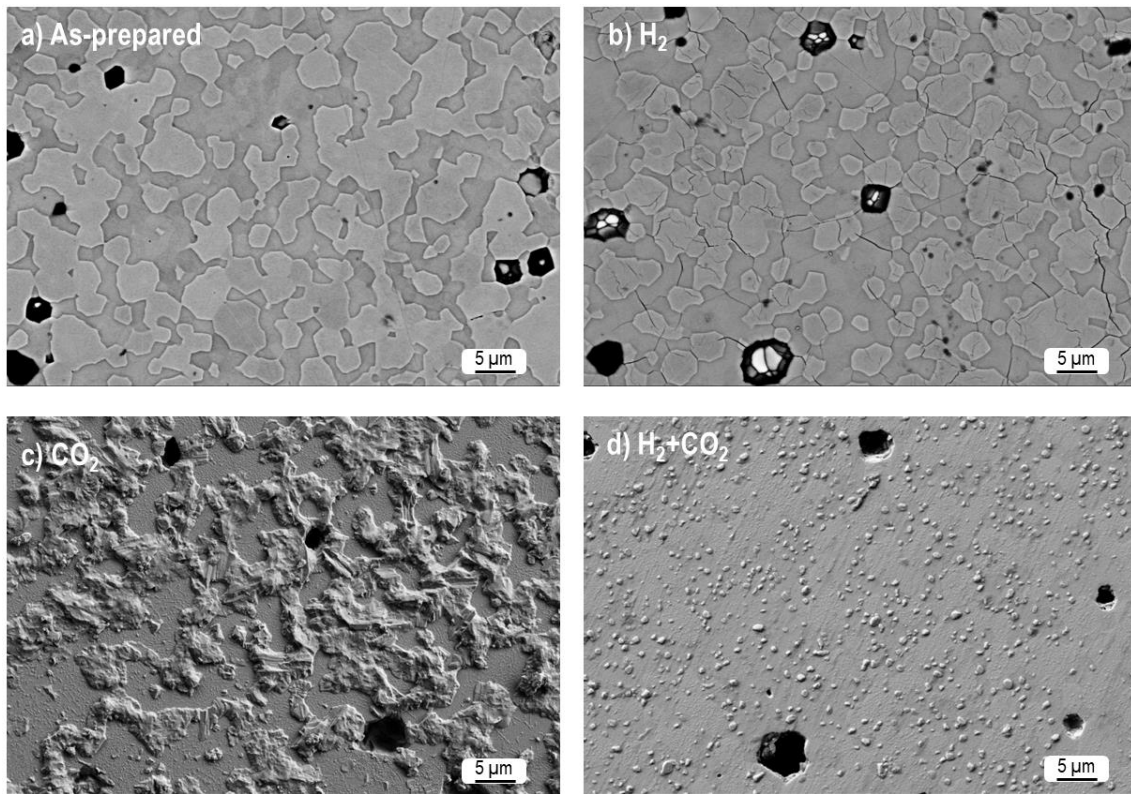
394 To better understand this behaviour, SEM analyses were performed onto the upper surfaces  
 395 (indented side) (Figure 7), and onto polished fracture surfaces (Figure 8) of the as-prepared and  
 396 thermally aged BCZY-GDC pellets (symmetric membranes). It is evident in this case that the  
 397 operating atmosphere strongly affects the microstructures of the membranes.

398 As shown in Figure 7b and 8b, the H<sub>2</sub> atmosphere leads to the formation of micro cracks,  
 399 concentrated in the GDC grains (lighter ones). This phenomenon is caused by the abovementioned  
 400 chemical expansion/contraction of the GDC cell after the aging cycle. Differently from the  
 401 asymmetric structure, the membranes in form of pellets are constituted by a less porous  
 402 microstructure with larger BCZY and GDC grains, because of the different production process (i.e.  
 403 tape casting and die pressing respectively). For these reasons, the effects of volume cell variations

404 are more pronounced and detectable at the microscopic level. However, it is worth to highlight that  
405 the extended cracks observed in Fig. 7b are detectable only onto the aged-surface level. On the  
406 contrary, microcracks are well-confined inside the GDC grains for the bulk of the pellet.

407 When the BCZY-GDC pellets are exposed to CO<sub>2</sub> atmosphere, the formation/emerging of BaCO<sub>3</sub>  
408 “islands” of sharpened-cornered grain microstructure is observed at the upper surface of the  
409 membrane (Figure 7c). This is in contrast with what observed on the dense active layer surface of  
410 the asymmetric membrane for which a uniform coating of BaCO<sub>3</sub> was clearly observed (Figure 5c).  
411 Moreover, the fracture surface reported in Figures 8c and S3a shows that the BCZY-CO<sub>2</sub> reaction  
412 occurs only at the first  $3.8 \pm 0.6 \mu\text{m}$  in thickness, as clearly determined by C-, Ba-, Gd-EDS profiles  
413 (Figure S3a). This confirms the key-role of the membrane architecture: while the carbonation  
414 reaction drastically affects the whole asymmetric membrane due to the open porous structure, the  
415 BCZY-GDC pellets are only aged at the surface level. The latter is confirmed by the calculated  
416  $0.0165 \pm 0.0007 \text{ wt\%}$  of CO<sub>2</sub> uptake corresponding to the formation of  $0.07 \pm 0.003 \text{ wt\%}$  of BaCO<sub>3</sub>.

417 Finally, as observed for the asymmetric structure, the aging in H<sub>2</sub>+CO<sub>2</sub> also causes the formation of  
418 larger BaCO<sub>3</sub> (micrometric in size) (Figure 7d), that could be seen as the early stage of the BaCO<sub>3</sub>  
419 “islands” structures formation observed for surface aged in pure CO<sub>2</sub>. The cross section of the  
420 BCZY-GDC pellet treated in H<sub>2</sub>+CO<sub>2</sub> (Figures 8d and S3b) shows no appreciable microstructural  
421 variations. Indeed, in this case, no weight variation (i.e. below detection limit) associated to CO<sub>2</sub>  
422 uptake was registered for the symmetric membranes before and after the aging treatment.



423

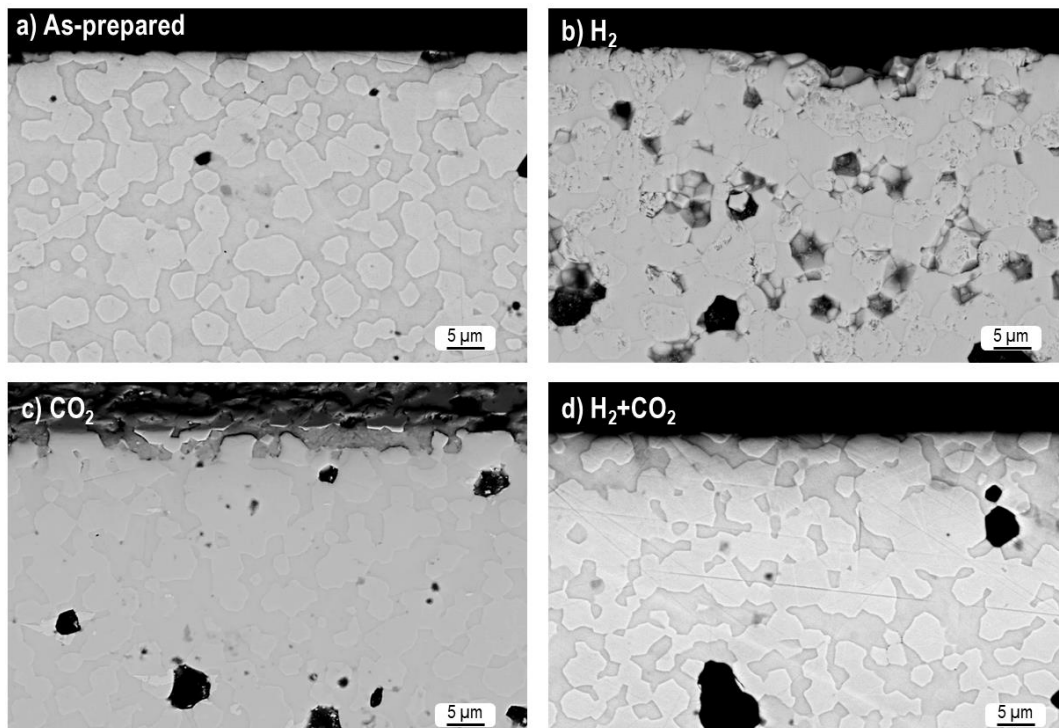
424

425

426

427

**Figure 7** SEM micrographs of the upper surfaces of symmetric BCZY-GDC membranes (pellets) after thermally aged at 750 °C for 100 h in different atmospheres: as-prepared (a), H<sub>2</sub> (b), CO<sub>2</sub> (c), H<sub>2</sub>+CO<sub>2</sub> (d).

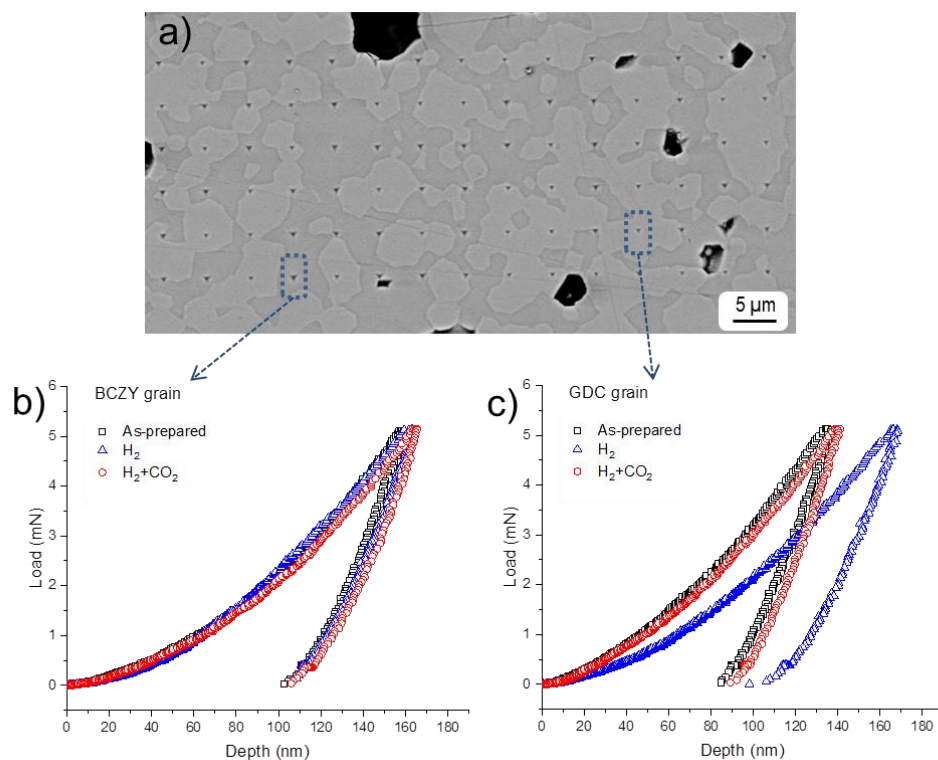


428

429 **Figure 8** SEM micrographs of the polished fracture surfaces of symmetric BCZY-GDC membranes  
430 (pellets) thermally aged at 750 °C for 100 h in different atmospheres: as-prepared (a), H<sub>2</sub> (b), CO<sub>2</sub>  
431 (c), H<sub>2</sub>+CO<sub>2</sub> (d).

432

433 To detect the hardness of the single perovskite and fluorite phases, nanoindentation tests were  
434 performed onto the polished surface of BCZY-GDC pellets (Figure 9 a) before and after the thermal  
435 aging in different atmospheres. Note that for the sample aged in CO<sub>2</sub> atmosphere, due to the lack of  
436 planarity caused by the formation/emerging of BaCO<sub>3</sub> “islands”, no reliable results could be  
437 registered. As shown in Figure 9b and 9c, load-displacement curves were acquired for both BCZY  
438 and GDC phases.



439

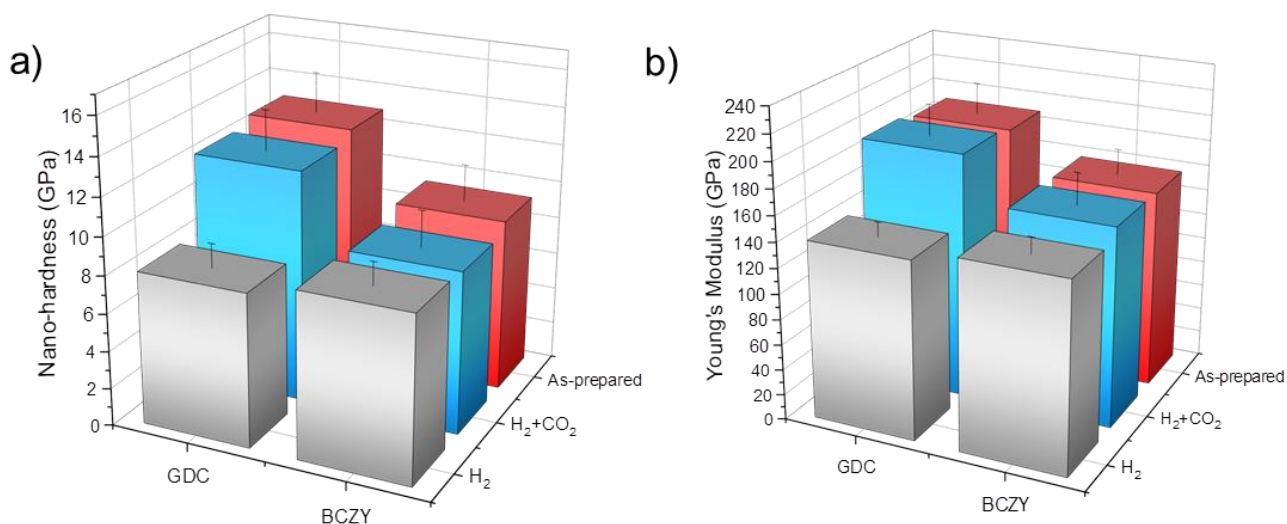
440 **Figure 9** a) BSE-SEM micrograph of the BCZY-GDC membrane (pellet) surface exposed to the  
441 aging atmosphere with the corresponding 90 nano-indentations. Load-displacement curves for b)  
442 BCZY and c) GDC grains before and after thermal aging at 750 °C for 100 h in H<sub>2</sub> and H<sub>2</sub>+CO<sub>2</sub>

443 atmosphere. Note that the load-displacement curves were not registered for membranes aged in CO<sub>2</sub>  
444 due to lack of planarity caused by the formation/emerging of BaCO<sub>3</sub> “islands” (Figure 8).

445

446 The nano-hardness and Young’s Modulus values extracted from the load-displacement curves are  
447 plotted in Figure 10 a) and b). The as-prepared composite is constituted by GDC and BCZY phases  
448 with calculated nano-hardness of  $12.8 \pm 2.1$  GPa and  $9.2 \pm 1.9$  GPa respectively. These data are  
449 consistent to the ones reported in previous works [41–43]. When the membrane is exposed to  
450 H<sub>2</sub>+CO<sub>2</sub>, no evident variation in nano-hardness is registered for the BCZY and GDC phases,  
451 confirming the hardness results previously described, whereas the thermal aging in H<sub>2</sub> atmosphere  
452 strongly affects the GDC nano-hardness. Its decrease is once again associated to the micro-cracking  
453 phenomenon already observed through SEM analyses, thus proving the issue associated to cycling  
454 treatments in these conditions. The trends registered for the Young’s Modulus (Figure 10 b)) are in  
455 accordance with the ones showed for nano-hardness.

456



457 **Figure 10** Nano-hardness a) and Young’s Modulus values b) determined for each of the two phases  
458 constituting the composite membrane (BCZY and GDC) determined through nano-indentation tests  
459 onto the pellets surface before and after the aging treatments.  
460



461

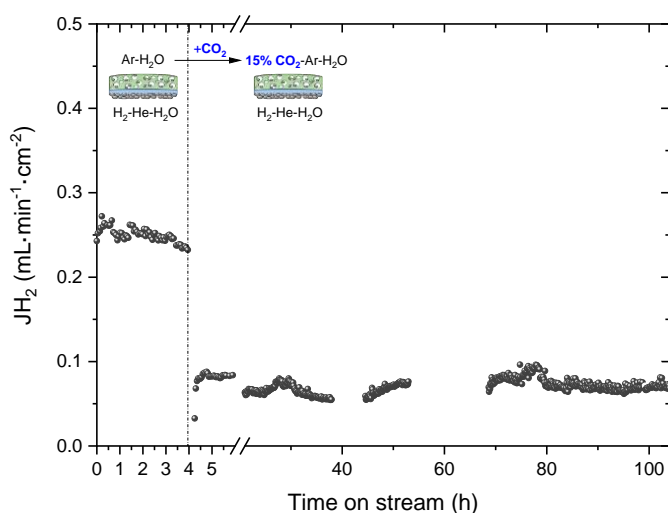
### 462 3.4 Hydrogen permeation test and post-mortem analyses.

463 Hydrogen permeation stability of the as-prepared asymmetric BCZY-GDC membrane, with a dense  
464 active layer  $18.7 \pm 1.2 \mu\text{m}$  thick, was evaluated for 100 h by using as sweep side an atmosphere  
465 composed by 15 vol%  $\text{CO}_2$  in Ar ( $135 \text{ mL}\cdot\text{min}^{-1}$ ) at  $750^\circ\text{C}$ . Sweep gas was fed on the porous  
466 substrate side (permeate side), and the  $\text{H}_2/\text{He}$  mixture was fed on the dense membrane layer side.

467 Figure 11 plots the  $\text{H}_2$  permeation values as a function of time on stream. First, the permeation test  
468 was carried out for 4 h by using Ar as sweep gas. Note that this composite possesses an important  
469 protonic conductivity but also oxygen ionic transport under the studied conditions. Then, the  $\text{H}_2$  flux  
470 observed is due to two different transport mechanisms: (i)  $\text{H}_2$  permeating through the membrane and  
471 (ii)  $\text{H}_2$  produced via water splitting due to the oxygen transport from the permeation side to the feed  
472 side. The sweep gas was then switched to 15 vol%  $\text{CO}_2$  in Ar stream.  $\text{H}_2$  permeation flux values  
473 steeply decrease when  $\text{CO}_2$  was added in the sweep gas and then remain stable for 100 h. No products  
474 formation or decrease of the  $\text{CO}_2$  concentration was observed by the GC analysis, indicating that  $\text{H}_2$   
475 and  $\text{CO}_2$  does not react. The  $\text{H}_2$  flux decrease agrees with that observed in a previous work for BCZY–  
476 GDC bulk membranes [15] and the protonic material  $\text{La}_{5.5}\text{WO}_{11.25-\delta}$  [44] and it is ascribed to the  
477  $\text{CO}_2/\text{O}_2$  competitive adsorption on the membrane surface that gives rise to the decrease of the  $\text{H}_2$   
478 formation via water splitting.  $\text{CO}_2/\text{O}_2$  competitive adsorption is reported for oxygen separation  
479 membranes based on  $\text{SrCo}_x\text{Fe}_{0.9-x}\text{Nb}_{0.1}\text{O}_{3-\delta}$  [45] where the drop of  $\text{O}_2$  permeation flux is ascribed to  
480 two different phenomenon: (1)  $\text{CO}_2$  chemical adsorption that provokes an instantaneous drop and  
481 agrees with the behavior observed in this work and; (2) reaction between  $\text{CO}_2$  and the ceramic  
482 material that is characterized by a continuous drop in permeation. In our study, the lowering of the  
483 permeation flux is attributed to the mechanism described in point (1).

484 On the other hand, the lower  $\text{H}_2$  fluxes ( $0.25 \text{ mL}\cdot\text{min}^{-1}\cdot\text{cm}^{-2}$  when only Ar is fed in the sweep side)  
485 as compared with previous studies ( $0.68 \text{ mL}\cdot\text{min}^{-1}\cdot\text{cm}^{-2}$ ) by using a similar membrane [14] are

486 ascribed to the concentration polarization resistance in the porous substrate as Ar and CO<sub>2</sub> were fed  
487 in the porous support side (whereas in the previous study H<sub>2</sub> and He were fed in the porous  
488 support), where molecular diffusion is the predominant transport mechanism, and both gases  
489 possess higher kinetic diameter than H<sub>2</sub> and He. Note that small oscillations/scattering observed in  
490 the permeation values may be due to the variations in the temperature of the water saturator (room  
491 temperature).

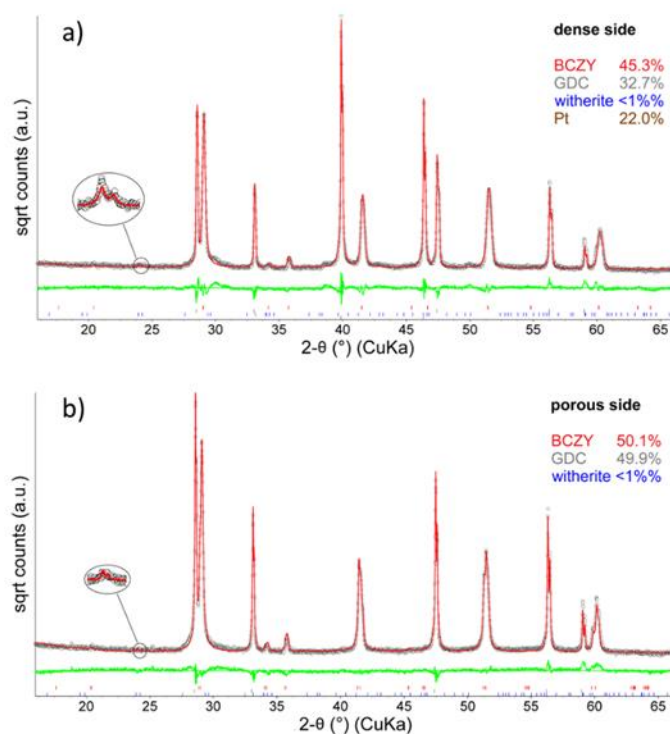


492 **Figure 11** H<sub>2</sub> permeation values as a function of time on stream by using wet Ar and 15 vol% CO<sub>2</sub>  
493 in Ar as sweep gas. Line indicates the addition of CO<sub>2</sub> to the sweep.  
494

495 After permeation measurements using CO<sub>2</sub> in the sweep gas for 100 h, the membranes were  
496 investigated through XRD and SEM analyses to assess any morphological and/or compositional  
497 modifications.

498 The XRD plots and Rietveld refinement results shown in Figure 12 and Table S1 respectively,  
499 confirm the preservation of the perovskite and fluorite phases, with detectable traces of witherite  
500 BaCO<sub>3</sub> (< 1 wt%). This is in accordance with the results obtained for the asymmetric membrane  
501 aged in H<sub>2</sub>+CO<sub>2</sub> atmosphere (for which the aging conditions were selected to mimic the ones the  
502 permeation test), previously discussed.

503



504

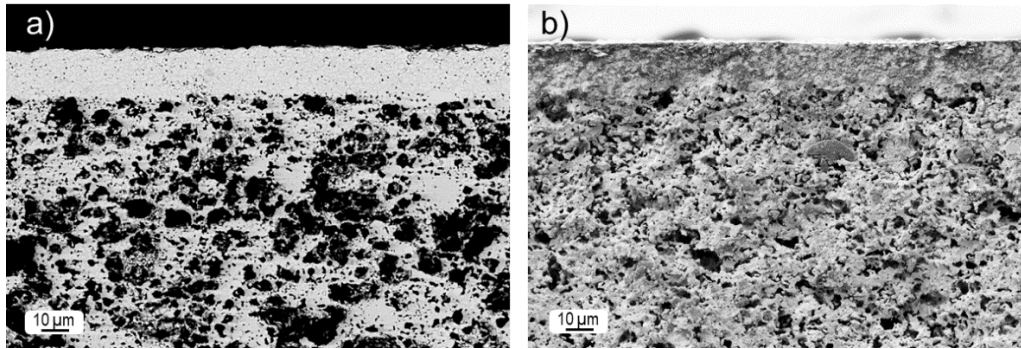
505 **Figure 12** XRD patterns of the BCZY-GDC membrane on both dense (a) and porous (b) sides of  
 506 the membrane (exposed to feed (a) and sweep stream (b)) after permeation measurements.

507

508 Comparing the microstructural characterization of the as-prepared membrane (Figure 4a) with the  
 509 post-mortem results (Figure 13a and S4b), it is evident that no detectable morphological and  
 510 compositional alterations occurred during permeation tests.

511 No cracks were in fact discernible into the fresh cross section of the membrane, while EDS profiles  
 512 (Figure S4b) for barium and gadolinium demonstrate that the homogeneous distribution of the  
 513 fluorite and perovskite phases is preserved. On the other hand, EDS profile of carbon (Figure S4a)  
 514 confirms the lack of detectable carbonated species after the permeation test using CO<sub>2</sub>.

515 Finally, the SEM micrographs of the fresh fracture depicted in Figure S4b show that the Pt  
 516 nanoparticles maintained their morphology and distribution through the BCZY-GDC porous  
 517 support.



518

519

520

521

522

523

524

525

526

527

528

529

**Figure 13** SEM micrographs of the asymmetric BCZY-GDC asymmetric membrane after permeation measurements: a) polished cross section and b) fracture surface.

It is important to notice that the  $H_2$  flux achieved in this work for is very promising considering the ones reported in literature (Table 3), especially among the ceramic-ceramic composite membranes. Even if the influence of the  $CO_2$  atmosphere on the hydrogen permeation performances is generally reported, very few information is available concerning the membrane mechanical stability after a prolonged operating condition. Therefore, the results obtained in this work demonstrate the general good stability of these systems under  $H_2+CO_2$  atmosphere, even for long-time operation (100 h) with promising permeation fluxes.

**Table 3** Summary of hydrogen performances for membranes tested in CO<sub>2</sub> atmosphere.

Membrane composition	Architecture	Thickness (μm)	Temperature (°C)	H <sub>2</sub> flux (mL min <sup>-1</sup> cm <sup>-2</sup> )	Feed (a)/sweep (b)	Phase and morphology stability	Thermo-Mechanical properties
<i>Ceramic-Metallic composite</i>							
Pd-Y <sub>2</sub> O <sub>3</sub> -stabilized ZrO <sub>2</sub> , 60:40 vol% [46]	Asymmetric planar structure	18	400-500	≈10 for 120 days	(a) 50% H <sub>2</sub> , 30% CO <sub>2</sub> , 1% CO, 3% H <sub>2</sub> O, 16% He, 500 mL min <sup>-1</sup> (b) N <sub>2</sub> ≈ 500 mL min <sup>-1</sup>	Not reported	Not reported
Ni-Ba(Zr <sub>0.1</sub> Ce <sub>0.7</sub> Y <sub>0.2</sub> )-O <sub>3-d</sub> , 40:60 vol% [47]	Symmetric pellet	266	900	0.35 for 80 h	(a) wet 20% CO <sub>2</sub> , 80% H <sub>2</sub> -He (40-60) (b) 100 ppm H <sub>2</sub> /N <sub>2</sub>	Sufficient stability verified by SEM in [48]	Not reported
Ni-BaZr <sub>0.1</sub> Ce <sub>0.7</sub> Y <sub>0.1</sub> Yb <sub>0.1</sub> O <sub>3-δ</sub> (, 40:60 vol% [49]	Symmetric pellet	560	900	0.0625	(a) wet 20% H <sub>2</sub> , 60% CO <sub>2</sub> , 20% He, 100 mL min <sup>-1</sup> (b) N <sub>2</sub>	BaCO <sub>3</sub> formation due to the degradation of Ni-BaZr <sub>0.1</sub> Ce <sub>0.7</sub> Y <sub>0.1</sub> Yb <sub>0.1</sub> O <sub>3-δ</sub> .	Not reported
Ni- Ba(Zr <sub>0.7</sub> Pr <sub>0.1</sub> Y <sub>0.2</sub> )O <sub>3</sub> , 40:60 vol% [50]	Symmetric pellet	400	850	0.008 for 40h	(a) wet 30% CO <sub>2</sub> , 70% H <sub>2</sub> -He (40-60) (b) Ar 20 mL min <sup>-1</sup>	Stable verified by XRD and SEM	Little cracks are found in the Ni or Ba(Zr <sub>0.7</sub> Pr <sub>0.1</sub> Y <sub>0.2</sub> )O <sub>3</sub> surface of particles due to lattice expansion
Ba <sub>0.95</sub> Ce <sub>0.85</sub> Tb <sub>0.05</sub> Zr <sub>0.1</sub> O <sub>3-δ</sub> / Ni-Ba <sub>0.95</sub> Ce <sub>0.85</sub> Tb <sub>0.05</sub> Zr <sub>0.1</sub> O <sub>3-δ</sub> (40-60 wt%) [51]	Asymmetric Hollow fiber	14	800	0.3 for 25 days	(a) 50 vol% H <sub>2</sub> / 50 vol% He, with a flow rate of 80 mL min <sup>-1</sup> (b)7 vol% of CO <sub>2</sub> in N <sub>2</sub> as sweep gas at flow rate 80 mL min <sup>-1</sup> ).	Stable verified by XRD and SEM	TEC evaluations in air. Sufficient matching
BaCe <sub>0.8</sub> Y <sub>0.2</sub> O <sub>3-δ</sub> - Ce <sub>0.8</sub> Y <sub>0.2</sub> O <sub>2-δ</sub> (28.6-71.4 wt%) / BaCe <sub>0.8</sub> Y <sub>0.2</sub> O <sub>3-δ</sub> - Ce <sub>0.8</sub> Y <sub>0.2</sub> O <sub>2-δ</sub> (90-10 wt%) [38]	Asymmetric Hollow fiber	17	850	1.34 for 125 h	50 vol% H <sub>2</sub> / 50 vol% He, 100 mL min <sup>-1</sup> (b) 7% CO <sub>2</sub> -N <sub>2</sub> , 80 mL min <sup>-1</sup>	Stable verified by XRD and SEM	TEC evaluations in air reported in [52]. Good thermal expansion matching

*Ceramic-ceramic composite*

$\text{SrCe}_{0.95}\text{Y}_{0.05}\text{O}_{3-\delta} - \text{ZnO}$ (90-10 wt%) [9]	Symmetric pellet	1100		0.002 for 24h	(a) 20 vol% $\text{H}_2$ / 80 vol% He, 80 $\text{mL min}^{-1}$ (b) 100 $\text{mL min}^{-1}$ $\text{CO}_2$ and 120 $\text{mL min}^{-1}$ $\text{N}_2$	Unstable ( $\text{CeO}_2$ , $\text{CeZn}_5$ and $\text{Sr}_2\text{CeO}_4$ formation) verified by XRD, SEM and TEM	Not reported
$\text{La}_{5.5}\text{WO}_{11.25-4}$ $\text{La}_{0.87}\text{Sr}_{0.13}\text{CrO}_{3-\delta}$ 50-50 vol% [10]	Symmetric pellet	370-600	850	0.075 for 24h	(a) Wet 50 vol.% $\text{H}_2$ in He 100 $\text{mL min}^{-1}$ for feed (b) Wet 15 vol.% $\text{CO}_2$ in Ar 150 $\text{mL min}^{-1}$	Stable verified by TG analysis	Not reported
$\text{BaCe}_{0.65}\text{Zr}_{0.20}\text{Y}_{0.15}\text{O}_{3-\delta} - \text{Ce}_{0.8}\text{Gd}_{0.2}\text{O}_{2-\delta}$ 50-50 vol% [15]	Symmetric pellet	660	750	$\approx 0.01$ for 24h	(a) Wet 50% vol $\text{H}_2$ in He (100 $\text{mL min}^{-1}$ ) (b) Wet 15 vol.% $\text{CO}_2$ in Ar 150 $\text{mL min}^{-1}$ for sweep	Stable verified by XRD, SEM and TG	Not reported
$\text{BaCe}_{0.65}\text{Zr}_{0.20}\text{Y}_{0.15}\text{O}_{3-\delta} - \text{Ce}_{0.8}\text{Gd}_{0.2}\text{O}_{2-\delta}$ 50-50 vol% THIS WORK	Asymmetric planar structure	19	750	$\approx 0.08$ for 100h	(a) Wet 50% vol $\text{H}_2$ in He (100 $\text{mL min}^{-1}$ ) (b) Wet 15 vol.% $\text{CO}_2$ in Ar 135 $\text{mL min}^{-1}$ for sweep	Stable verified by XRD and SEM	Good mechanical stability in terms of flexural strength and hardness after operating cycle.
$\text{BaCe}_{0.8}\text{Eu}_{0.2}\text{O}_{3-\delta} - \text{Ce}_{0.8}\text{Y}_{0.2}\text{O}_{2-\delta}$ 50-50 vol% [11]	Symmetric pellet	500	700	$\approx 0.14$ for 140h	(a) Wet 50 vol.% $\text{H}_2$ in He 100 $\text{mL min}^{-1}$ for feed (b) Wet 15 vol.% $\text{CO}_2$ in Ar 150 $\text{mL min}^{-1}$ for sweep	Stable verified by XRD, SEM and TG	TEC evaluations in air. No cracks evaluated after thermochemical cycles
$\text{SrCe}_{0.95}\text{Fe}_{0.05}\text{O}_{3-\delta} - \text{SrCe}_{0.05}\text{Fe}_{0.95}\text{O}_{3-\delta}$ [53]	Symmetric pellet	700	900	0.25 (10% $\text{CO}_2$ ) for 30h	40% $\text{H}_2$ /wet Ar, 10% $\text{CO}_2$	Not presented	Non reported
$\text{Ce}_{0.90}\text{Gd}_{0.10}\text{O}_{3-\delta} - \text{SrCe}_{0.95}\text{Fe}_{0.05}\text{O}_{3-\delta} - \text{SrFe}_{0.95}\text{Ce}_{0.05}\text{O}_{3-\delta}$ [54]	Symmetric pellet	700	940	0.33 (10% $\text{CO}_2$ ) for 30h	40% $\text{H}_2$ /wet Ar, 10% $\text{CO}_2$	Severe decomposition in $\text{SrCO}_3$ , $\text{CeO}_2$ and $\text{Sr}_2\text{FeO}_4$ , confirming the formation of carbonates for Sr-based sample under $\text{CO}_2$ atmospheres.	Non reported

## Conclusions

The influence of thermal aging treatments (100 h at the selected operating temperature of 750 °C) in different atmospheres ( $H_2$ ,  $CO_2$ ,  $H_2+CO_2$ ) on the long-term microstructural and mechanical stability of BCZY-GDC membranes was deeply investigated. Either tape-cast asymmetric membranes (porous substrate supporting the dense active layer), or pellets (symmetric configuration) were considered.

The exposure of the membrane to  $H_2$ -atmosphere leads to lower flexural strength values, i.e. 22 MPa with respect to 70 MPa of the as-prepared membrane. This is caused by a general embrittlement of the asymmetric structure, due to chemical expansion/contraction of the GDC cell after the aging cycle. Indeed, micro-cracking of GDC grains is clearly observed in symmetric membranes. This phenomenon causes the decrease of GDC nano-hardness value from 12.8 (for the as-prepared membrane) to 8.8 GPa, impacting, therefore, the composite Vickers hardness value, i.e. 354 Hv with respect to 543 Hv of the as-prepared membrane.

The aging in  $CO_2$  atmosphere causes a slightly increase in flexural strength values (81 MPa) due to the formation, especially in the porous support, of ZrO<sub>2</sub>-BaCO<sub>3</sub> sub-micrometric phases at the expense of the almost total amount of perovskite, strengthening the membrane microstructure. Higher hardness values (704 Hv) were also recorded due to the emerging of BaCO<sub>3</sub> islands on the symmetric membrane surface due to the same toughening mechanism of the matrix by sub-micrometric particles. It is worth to notice, however, that the carbonation reaction drastically affects the whole asymmetric membrane due to the open porous structure, while the BCZY-GDC pellets are only aged at the surface level, confirming the key-role of the membrane architecture.

The membrane aged for 100 h in the operating  $H_2+CO_2$  atmosphere shows only a slight decrease in flexural strength and comparable hardness values because no evident morphological or structural

changes (except the BaCO<sub>3</sub> formation in trace amount) were observed, regardless the membrane configuration.

Finally, promising and stable hydrogen permeation flux values were obtained on the asymmetric membrane at 750 °C, for 100 h, using wet 15 vol% CO<sub>2</sub> in Ar as sweep gas. Neither structural nor morphological modifications of the membrane were detected after the testing, confirming the results registered for the membrane aged in similar conditions (750 °C, H<sub>2</sub>+CO<sub>2</sub> atmosphere). Further work is required to improve the catalytic activity of the support and minimize gas diffusion resistance through the porous media to implement the final hydrogen permeation. Nonetheless, the present results confirm the high potentiality of proton-ceramic membranes based on BCZY-GDC composite thanks to the encouraging hydrogen fluxes, microstructural and mechanical stability in operating atmospheres containing CO<sub>2</sub>. This is therefore a further essential step towards the future industrialization of these systems in line with the objective defined by the “European Green Deal”.

### **Conflicts of interest**

There are no conflicts of interest to declare.

### **Acknowledgements**

This work was financially supported by the agreement between the Italian Ministry of Economic Development and the Italian National Research Council “Ricerca di sistema elettrico nazionale” and by the Spanish Government (RTI2018-102161) and the Generalitat Valenciana (PROMETEO/2018/006).



## References

- [1] The European Green Deal: hydrogen is a priority area for a clean and circular economy | [www.fch.europa.eu](http://www.fch.europa.eu), (n.d.). <https://www.fch.europa.eu/news/european-green-deal-hydrogen-priority-area-clean-and-circular-economy> (accessed June 4, 2021).
- [2] W. Deibert, M.E. Ivanova, S. Baumann, O. Guillon, W.A. Meulenber, Ion-conducting ceramic membrane reactors for high-temperature applications, *Journal of Membrane Science*. 543 (2017) 79–97. <https://doi.org/10.1016/j.memsci.2017.08.016>.
- [3] S.H. Morejudo, R. Zanón, S. Escolástico, I. Yuste-Tirados, H. Malerød-Fjeld, P.K. Vestre, W.G. Coors, A. Martínez, T. Norby, J.M. Serra, C. Kjølseth, Direct conversion of methane to aromatics in a catalytic co-ionic membrane reactor, *Science*. 353 (2016) 563–566. <https://doi.org/10.1126/science.aag0274>.
- [4] H. Malerød-Fjeld, D. Clark, I. Yuste-Tirados, R. Zanón, D. Catalán-Martinez, D. Beeaff, S.H. Morejudo, P.K. Vestre, T. Norby, R. Haugsrud, J.M. Serra, C. Kjølseth, Thermo-electrochemical production of compressed hydrogen from methane with near-zero energy loss, *Nat Energy*. 2 (2017) 923–931. <https://doi.org/10.1038/s41560-017-0029-4>.
- [5] N.A. Al-Mufachi, N.V. Rees, R. Steinberger-Wilkens, Hydrogen selective membranes: A review of palladium-based dense metal membranes, *Renewable and Sustainable Energy Reviews*. 47 (2015) 540–551. <https://doi.org/10.1016/j.rser.2015.03.026>.
- [6] G. Bernardo, T. Araújo, T. da Silva Lopes, J. Sousa, A. Mendes, Recent advances in membrane technologies for hydrogen purification, *International Journal of Hydrogen Energy*. 45 (2020) 7313–7338. <https://doi.org/10.1016/j.ijhydene.2019.06.162>.
- [7] S.S. Hashim, M.R. Somalu, K.S. Loh, S. Liu, W. Zhou, J. Sunarso, Perovskite-based proton conducting membranes for hydrogen separation: A review, *International Journal of Hydrogen Energy*. 43 (2018) 15281–15305. <https://doi.org/10.1016/j.ijhydene.2018.06.045>.
- [8] H. Wang, X. Wang, B. Meng, X. Tan, K.S. Loh, J. Sunarso, S. Liu, Perovskite-based mixed protonic–electronic conducting membranes for hydrogen separation: Recent status and advances, *Journal of Industrial and Engineering Chemistry*. 60 (2018) 297–306. <https://doi.org/10.1016/j.jiec.2017.11.016>.
- [9] T. Wang, H. Zhang, B. Meng, X. Wang, J. Sunarso, X. Tan, S. Liu, SrCe<sub>0.95</sub>Y<sub>0.05</sub>O<sub>3-δ</sub>–ZnO dual-phase membranes for hydrogen permeation, *RSC Adv*. 6 (2016) 36786–36793. <https://doi.org/10.1039/C6RA02921C>.
- [10] S. Escolástico, C. Solís, C. Kjølseth, J.M. Serra, Outstanding hydrogen permeation through CO<sub>2</sub>-stable dual-phase ceramic membranes, *Energy Environ. Sci*. 7 (2014) 3736–3746. <https://doi.org/10.1039/C4EE02066A>.
- [11] M.E. Ivanova, S. Escolástico, M. Balaguer, J. Palisaitis, Y.J. Sohn, W.A. Meulenber, O. Guillon, J. Mayer, J.M. Serra, Hydrogen separation through tailored dual phase membranes with nominal composition BaCe<sub>0.8</sub>Eu<sub>0.2</sub>O<sub>3-δ</sub>:Ce<sub>0.8</sub>Y<sub>0.2</sub>O<sub>2-δ</sub> at intermediate temperatures, *Sci Rep*. 6 (2016) 34773. <https://doi.org/10.1038/srep34773>.
- [12] J.M. Polfus, W. Xing, M.-L. Fontaine, C. Denonville, P.P. Henriksen, R. Bredesen, Hydrogen separation membranes based on dense ceramic composites in the La<sub>27</sub>W<sub>5</sub>O<sub>55.5</sub>–LaCrO<sub>3</sub> system, *Journal of Membrane Science*. 479 (2015) 39–45. <https://doi.org/10.1016/j.memsci.2015.01.027>.
- [13] J. S. Fish, S. Ricote, R. O’Hayre, N. Bonanos, Electrical properties and flux performance of composite ceramic hydrogen separation membranes, *Journal of Materials Chemistry A*. 3 (2015) 5392–5401. <https://doi.org/10.1039/C5TA00450K>.
- [14] D. Montaleone, E. Mercadelli, S. Escolástico, A. Gondolini, J.M. Serra, A. Sanson, All-ceramic asymmetric membranes with superior hydrogen permeation, *J. Mater. Chem. A*. 6 (2018) 15718–15727. <https://doi.org/10.1039/C8TA04764B>.
- [15] E. Rebollo, C. Mortalò, S. Escolástico, S. Boldrini, S. Barison, J.M. Serra, M. Fabrizio, Exceptional hydrogen permeation of all-ceramic composite robust membranes based on BaCe<sub>0.65</sub>Zr<sub>0.20</sub>Y<sub>0.15</sub>O<sub>3-δ</sub> and Y- or Gd-doped ceria, *Energy Environ. Sci*. 8 (2015) 3675–3686. <https://doi.org/10.1039/C5EE01793A>.
- [16] C. Mortalò, E. Rebollo, S. Escolástico, S. Deambrosis, K. Haas-Santo, M. Rancan, R. Dittmeyer, L. Armelao, M. Fabrizio, Enhanced sulfur tolerance of BaCe<sub>0.65</sub>Zr<sub>0.20</sub>Y<sub>0.15</sub>O<sub>3-δ</sub>–Ce<sub>0.85</sub>Gd<sub>0.15</sub>O<sub>2-δ</sub>

- composite for hydrogen separation membranes, *Journal of Membrane Science*. 564 (2018) 123–132. <https://doi.org/10.1016/j.memsci.2018.07.015>.
- [17] D. Montaleone, E. Mercadelli, A. Gondolini, P. Pinasco, A. Sanson, On the compatibility of dual phase BaCe<sub>0.65</sub>Zr<sub>0.2</sub>Y<sub>0.15</sub>O<sub>3-δ</sub>-based membrane for hydrogen separation application, *Ceramics International*. 43 (2017) 10151–10157. <https://doi.org/10.1016/j.ceramint.2017.05.039>.
- [18] E. Mercadelli, D. Montaleone, A. Gondolini, P. Pinasco, A. Sanson, Tape-cast asymmetric membranes for hydrogen separation, *Ceramics International*. 43 (2017) 8010–8017. <https://doi.org/10.1016/j.ceramint.2017.03.099>.
- [19] D. Montaleone, E. Mercadelli, A. Gondolini, M. Ardit, P. Pinasco, A. Sanson, Role of the sintering atmosphere in the densification and phase composition of asymmetric BCZY-GDC composite membrane, *Journal of the European Ceramic Society*. 39 (2019) 21–29. <https://doi.org/10.1016/j.jeurceramsoc.2018.01.043>.
- [20] E. Mercadelli, A. Gondolini, D. Montaleone, P. Pinasco, S. Escolástico, J.M. Serra, A. Sanson, Production strategies of asymmetric BaCe<sub>0.65</sub>Zr<sub>0.2</sub>Y<sub>0.15</sub>O<sub>3-δ</sub> – Ce<sub>0.8</sub>Gd<sub>0.2</sub>O<sub>2-δ</sub> membrane for hydrogen separation, *International Journal of Hydrogen Energy*. 45 (2020) 7468–7478. <https://doi.org/10.1016/j.ijhydene.2019.03.148>.
- [21] E. Mercadelli, A. Gondolini, D. Montaleone, P. Pinasco, A. Sanson, Innovative strategy for designing proton conducting ceramic tapes and multilayers for energy applications, *Journal of the European Ceramic Society*. 41 (2021) 488–496. <https://doi.org/10.1016/j.jeurceramsoc.2020.09.016>.
- [22] C. Mortalò, A. Santoru, C. Pistidda, E. Rebollo, M. Boaro, C. Leonelli, M. Fabrizio, Structural evolution of BaCe<sub>0.65</sub>Zr<sub>0.2</sub>Y<sub>0.15</sub>O<sub>3-δ</sub>-Ce<sub>0.85</sub>Gd<sub>0.15</sub>O<sub>2-δ</sub> composite MPEC membrane by in-situ synchrotron XRD analyses, *Materials Today Energy*. 13 (2019) 331–341. <https://doi.org/10.1016/j.mtener.2019.06.004>.
- [23] J. Malzbender, Mechanical aspects of ceramic membrane materials, *Ceramics International*. 42 (2016) 7899–7911. <https://doi.org/10.1016/j.ceramint.2016.02.136>.
- [24] L. Chen, L. Liu, J. Xue, L. Zhuang, H. Wang, Asymmetric membrane structure: An efficient approach to enhance hydrogen separation performance, *Separation and Purification Technology*. 207 (2018) 363–369. <https://doi.org/10.1016/j.seppur.2018.06.066>.
- [25] G. Pećanac, S. Baumann, J. Malzbender, Mechanical properties and lifetime predictions for Ba<sub>0.5</sub>Sr<sub>0.5</sub>Co<sub>0.8</sub>Fe<sub>0.2</sub>O<sub>3-δ</sub> membrane material, *Journal of Membrane Science*. 385–386 (2011) 263–268. <https://doi.org/10.1016/j.memsci.2011.10.005>.
- [26] G. Pećanac, S. Foghmoes, M. Lipińska-Chwałek, S. Baumann, T. Beck, J. Malzbender, Strength degradation and failure limits of dense and porous ceramic membrane materials, *Journal of the European Ceramic Society*. 33 (2013) 2689–2698. <https://doi.org/10.1016/j.jeurceramsoc.2013.04.018>.
- [27] M. Lipińska-Chwałek, G. Pećanac, J. Malzbender, Creep behaviour of membrane and substrate materials for oxygen separation units, *Journal of the European Ceramic Society*. 33 (2013) 1841–1848. <https://doi.org/10.1016/j.jeurceramsoc.2013.02.007>.
- [28] V.K. Stournari, Thermo-mechanical Properties of Mixed Ionic-Electronic Conducting Membranes for Gas Separation, *Forschungszentrum Jülich GmbH Zentralbibliothek, Verlag*, 2016. <https://juser.fz-juelich.de/record/283575> (accessed August 23, 2021).
- [29] V. Stournari, W. Deibert, M.E. Ivanova, C. Krautgasser, R. Bermejo, J. Malzbender, Mechanical properties of tape casted Lanthanum Tungstate for membrane substrate application, *Ceramics International*. 42 (2016) 15177–15182. <https://doi.org/10.1016/j.ceramint.2016.06.109>.
- [30] W. Deibert, V. Stournari, M.E. Ivanova, S. Escolástico, J.M. Serra, J. Malzbender, T. Beck, L. Singheiser, O. Guillon, W.A. Meulenbergh, Effect of microstructure on electrical and mechanical properties of La<sub>5.4</sub>WO<sub>12-δ</sub> proton conductor, *Journal of the European Ceramic Society*. 38 (2018) 3527–3538. <https://doi.org/10.1016/j.jeurceramsoc.2018.04.009>.
- [31] S. Escolástico, V. Stournari, J. Malzbender, K. Haas-Santo, R. Dittmeyer, J.M. Serra, Chemical stability in H<sub>2</sub>S and creep characterization of the mixed protonic conductor Nd<sub>5.5</sub>WO<sub>11.25-δ</sub>, (2018). <https://doi.org/10.1016/J.IJHYDENE.2018.03.060>.

- [32] Y. Guo, Y. Lin, R. Ran, Z. Shao, Zirconium doping effect on the performance of proton-conducting  $\text{BaZr}_{0.8-y}\text{Ce}_{0.2}\text{O}_{3-\delta}$  ( $0.0 \leq y \leq 0.8$ ) for fuel cell applications, *Journal of Power Sources*. 193 (2009) 400–407. <https://doi.org/10.1016/j.jpowsour.2009.03.044>.
- [33] N. Irani, H. Rezaie, R. Naghizadeh, Investigation on the effect of  $\text{BaCO}_3$  on the physical and mechanical properties of  $5\text{Ni}/10\text{NiO} \cdot \text{NiFe}_2\text{O}_4$  cermet, *Functional Composites and Structures*. 2 (2020). <https://doi.org/10.1088/2631-6331/ab9753>.
- [34] N. Bouzidi, A. Bouzidi, R.O. Nunes, D. Merabet, Study of the microstructure and mechanical properties of halloysite–kaolinite/ $\text{BaCO}_3$  ceramic composites, *Clay Minerals*. 53 (2018) 403–412. <https://doi.org/10.1180/clm.2018.29>.
- [35] H.A. Abdel-Gawwad, K.A. Metwally, T.A. Tawfik, Role of barium carbonate and barium silicate nanoparticles in the performance of cement mortar, *Journal of Building Engineering*. 44 (2021) 102721. <https://doi.org/10.1016/j.jobbe.2021.102721>.
- [36] M.F. Bekheet, M. Grünbacher, L. Schlicker, A. Gili, A. Doran, J.D. Epping, A. Gurlo, B. Klötzer, S. Penner, On the structural stability of crystalline ceria phases in undoped and acceptor-doped ceria materials under in situ reduction conditions, *CrystEngComm*. 21 (2018) 145–154. <https://doi.org/10.1039/C8CE01726C>.
- [37] D. Medvedev, J. Lyagaeva, S. Plaksin, A. Demin, P. Tsiakaras, Sulfur and carbon tolerance of  $\text{BaCeO}_3$ – $\text{BaZrO}_3$  proton-conducting materials, *Journal of Power Sources*. 273 (2015) 716–723. <https://doi.org/10.1016/j.jpowsour.2014.09.116>.
- [38] H. Cheng, B. Meng, X. Wang, X. Meng, S. Liu,  $\text{CO}_2$  and Steam-Assisted  $\text{H}_2$  Separation through  $\text{BaCe}_{0.8}\text{Y}_{0.2}\text{O}_{3-\delta}$ – $\text{Ce}_{0.8}\text{Y}_{0.2}\text{O}_{2-\delta}$  Hollow Fiber Membranes, *Energy Fuels*. 34 (2020) 683–689. <https://doi.org/10.1021/acs.energyfuels.9b02972>.
- [39] A.K.E. Andersson, S.M. Selbach, C.S. Knee, T. Grande, Chemical Expansion Due to Hydration of Proton-Conducting Perovskite Oxide Ceramics, *J. Am. Ceram. Soc.* 97 (2014) 2654–2661. <https://doi.org/10.1111/jace.12990>.
- [40] G. Hudish, A. Manerbino, W.G. Coors, S. Ricote, Chemical expansion in  $\text{BaZr}_{0.9-x}\text{Ce}_x\text{Y}_{0.1}\text{O}_{3-\delta}$  ( $x = 0$  and  $0.2$ ) upon hydration determined by high-temperature X-ray diffraction, *Journal of the American Ceramic Society*. 101 (2018) 1298–1309. <https://doi.org/10.1111/jace.15275>.
- [41] M. Morales, J.J. Roa, X.G. Capdevila, M. Segarra, S. Piñol, Mechanical properties at the nanometer scale of GDC and YSZ used as electrolytes for solid oxide fuel cells, *Acta Materialia*. 58 (2010) 2504–2509. <https://doi.org/10.1016/j.actamat.2009.12.036>.
- [42] P.-F. Yang, D.-L. Chen, S.-R. Jian, S.-W. Lee, C.-J. Tseng, Mechanical Properties of  $\text{Ba}_{1-x}\text{K}_x\text{Ce}_{0.6}\text{Zr}_{0.2}\text{Y}_{0.2}\text{O}_{3-\delta}$  Oxides by Nanoindentation, *Procedia Engineering*. 79 (2014) 599–605. <https://doi.org/10.1016/j.proeng.2014.06.385>.
- [43] W. Zhou, J. Malzbender, F. Zeng, W. Deibert, O. Guillon, R. Schwaiger, W.A. Meulenbergh, Mechanical properties of  $\text{BaCe}_{0.65}\text{Zr}_{0.2}\text{Y}_{0.15}\text{O}_{3-\delta}$  proton-conducting material determined using different nanoindentation methods, *Journal of the European Ceramic Society*. 40 (2020) 5653–5661. <https://doi.org/10.1016/j.jeurceramsoc.2020.07.044>.
- [44] S. Escolástico, C. Solís, T. Scherb, G. Schumacher, J.M. Serra, Hydrogen separation in  $\text{La}_{5.5}\text{WO}_{11.25-\delta}$  membranes, *Journal of Membrane Science*. 444 (2013) 276–284. <https://doi.org/10.1016/j.memsci.2013.05.005>.
- [45] Z. Wang, N. Dewangan, S. Das, M.H. Wai, S. Kawi, High oxygen permeable and  $\text{CO}_2$ -tolerant  $\text{SrCo}_x\text{Fe}_{0.9-x}\text{Nb}_{0.1}\text{O}_{3-\delta}$  ( $x = 0.1$ – $0.8$ ) perovskite membranes: Behavior and mechanism, *Separation and Purification Technology*. 201 (2018) 30–40. <https://doi.org/10.1016/j.seppur.2018.02.046>.
- [46] U. (Balu) Balachandran, T.H. Lee, C.Y. Park, J.E. Emerson, J.J. Picciolo, S.E. Dorris, Dense cermet membranes for hydrogen separation, *Separation and Purification Technology*. 121 (2014) 54–59. <https://doi.org/10.1016/j.seppur.2013.10.001>.
- [47] C. Zuo, T.H. Lee, S.E. Dorris, U. Balachandran, M. Liu, Composite  $\text{Ni}$ – $\text{Ba}(\text{Zr}_{0.1}\text{Ce}_{0.7}\text{Y}_{0.2})\text{O}_3$  membrane for hydrogen separation, *Journal of Power Sources*. 159 (2006) 1291–1295. <https://doi.org/10.1016/j.jpowsour.2005.12.042>.

- [48] C. Zuo, S.E. Dorris, U. Balachandran, M. Liu, Effect of Zr-Doping on the Chemical Stability and Hydrogen Permeation of the Ni–BaCe<sub>0.8</sub>Y<sub>0.2</sub>O<sub>3-α</sub> Mixed Protonic–Electronic Conductor, *Chem. Mater.* 18 (2006) 4647–4650. <https://doi.org/10.1021/cm0518224>.
- [49] S. Fang, K.S. Brinkman, F. Chen, Hydrogen permeability and chemical stability of Ni–BaZr<sub>0.1</sub>Ce<sub>0.7</sub>Y<sub>0.1</sub>Yb<sub>0.1</sub>O<sub>3-δ</sub> membrane in concentrated H<sub>2</sub>O and CO<sub>2</sub>, *Journal of Membrane Science.* 467 (2014) 85–92. <https://doi.org/10.1016/j.memsci.2014.05.008>.
- [50] Z. Zhu, W. Sun, Y. Dong, Z. Wang, Z. Shi, Q. Zhang, W. Liu, Evaluation of hydrogen permeation properties of Ni–Ba(Zr<sub>0.7</sub>Pr<sub>0.1</sub>Y<sub>0.2</sub>)O<sub>3-δ</sub> cermet membranes, *International Journal of Hydrogen Energy.* 39 (2014) 11683–11689. <https://doi.org/10.1016/j.ijhydene.2014.05.163>.
- [51] Y. Shang, L. Wei, X. Meng, B. Meng, N. Yang, J. Sunarso, S. Liu, CO<sub>2</sub>-enhanced hydrogen permeability of dual-layered A-site deficient Ba<sub>0.95</sub>Ce<sub>0.85</sub>Tb<sub>0.05</sub>Zr<sub>0.1</sub>O<sub>3-δ</sub>-based hollow fiber membrane, *Journal of Membrane Science.* 546 (2018) 82–89. <https://doi.org/10.1016/j.memsci.2017.10.012>.
- [52] H. Cheng, X. Wang, X. Meng, B. Meng, J. Sunarso, X. Tan, L. Liu, S. Liu, Dual-layer BaCe<sub>0.8</sub>Y<sub>0.2</sub>O<sub>3-δ</sub>-Ce<sub>0.8</sub>Y<sub>0.2</sub>O<sub>2-δ</sub>/BaCe<sub>0.8</sub>Y<sub>0.2</sub>O<sub>3-δ</sub>-Ni hollow fiber membranes for H<sub>2</sub> separation, *Journal of Membrane Science.* 601 (2020) 117801. <https://doi.org/10.1016/j.memsci.2019.117801>.
- [53] J. Lujian, S. Ashtiani, F. Liang, G. He, Hydrogen permeation through dual-phase ceramic membrane derived from automatic phase-separation of SrCe<sub>0.5</sub>Fe<sub>0.5</sub>O<sub>3-δ</sub> precursor, *International Journal of Hydrogen Energy.* 45 (2019). <https://doi.org/10.1016/j.ijhydene.2019.11.241>.
- [54] L. Jia, M. Liu, X. Xu, W. Dong, H. Jiang, Gd-doped ceria enhanced triple-conducting membrane for efficient hydrogen separation, *Separation and Purification Technology.* 256 (2021) 117798. <https://doi.org/10.1016/j.seppur.2020.117798>.

## Supporting information of “Chemical and mechanical stability of BCZY-GDC membranes for hydrogen separation”

**Table S1.** Refinement agreement factors, quantitative phase analysis and unit-cell parameters with their standard deviations for BCZY-GDC membrane on both dense (feed stream exposition) and porous (sweep stream exposition) sides of the membrane after permeation measurements. BCZY and GDC stand for  $\text{Ba}(\text{Ce}_{0.65}\text{Zr}_{0.2}\text{Y}_{0.15})\text{O}_{2.925}$  with perovskite structure and  $(\text{Ce}_{0.8}\text{Gd}_{0.2})\text{O}_{1.9}$  with fluorite-type structure, respectively.

	Phase	Wt%	s.g.	<i>a</i> (Å)	<i>b</i> (Å)	<i>c</i> (Å)	<i>V</i> (Å <sup>3</sup> )	<i>R</i> <sub>wp</sub>
dense feed stream	BCZY	45.3(1.0)	<i>Imma</i>	6.1464(3)	8.6981(5)	6.1509(3)	328.84(3)	0.122
	GDC	32.7(0.7)	<i>Fm-3m</i>	5.4194(1)	–	–	159.17(1)	
	Pt	22.0(1.7)	<i>Fm-3m</i>	3.9150(1)	–	–	60.01(1)	
	witherite	b.d.l.	<i>Pmcn</i>	–	–	–	–	
porous sweep stream	BCZY	50.1(1)	<i>Imma</i>	6.1832(2)	8.6893(4)	6.1568(1)	330.79(2)	0.106
	GDC	49.9(1)	<i>Fm-3m</i>	5.4217(1)	–	–	159.37(1)	

NOTE: Although identified in the dense side of the membrane exposed to a feed stream, witherite has not quantified as below detection limit (b.d.l.).

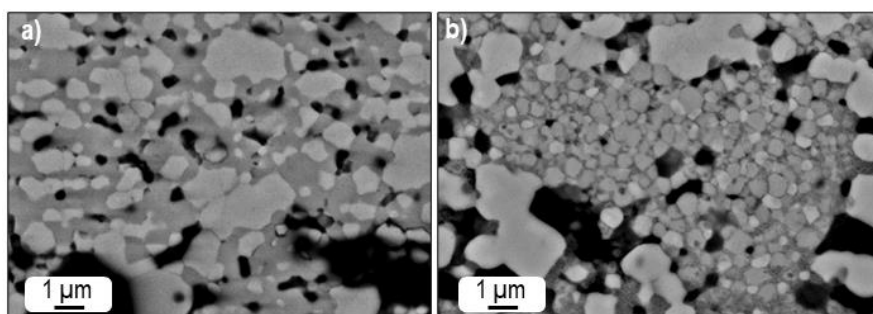


**Figure S1.** Details of the polished cross sections of the asymmetric membranes as-prepared (a) and aged at 750 °C for 100 h in CO<sub>2</sub> (b)

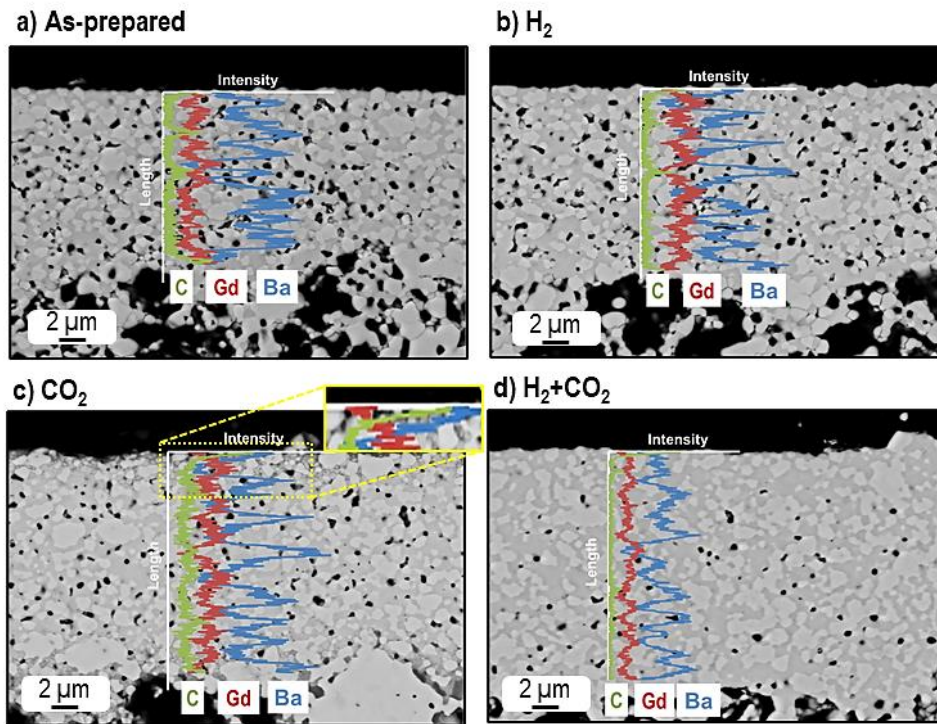


**Figure S2.** Ba/Gd/C EDS profiles along the dense membrane layer thickness of the polished cross sections of the asymmetric membranes aged at 750 °C for 100 h in different atmospheres: as-prepared (a), H<sub>2</sub> (b), CO<sub>2</sub> (c), H<sub>2</sub>+CO<sub>2</sub> (d)

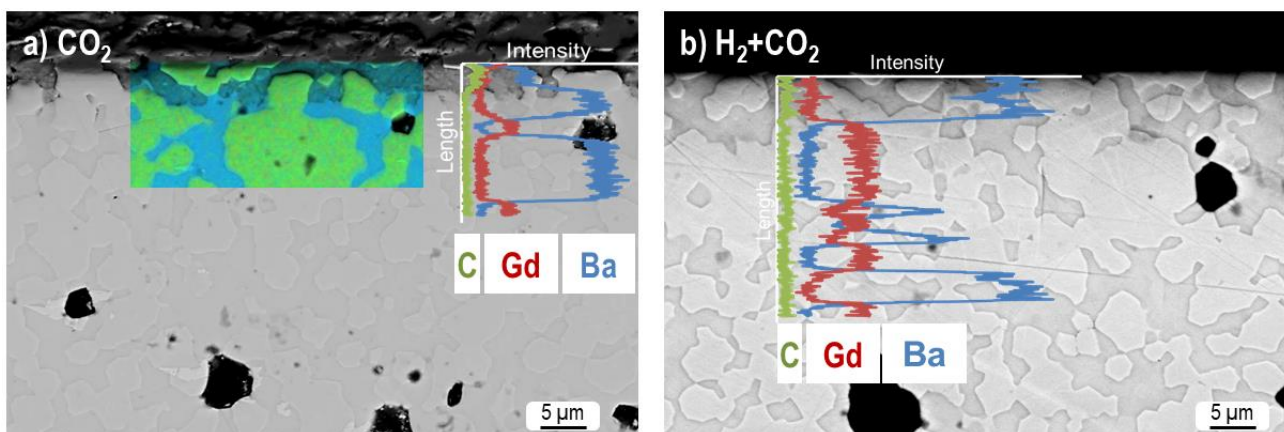


**Figure S3.** SEM micrographs of the polished fracture surfaces of symmetric BCZY-GDC membranes (pellets) thermally aged at 750 °C for 100 h in CO<sub>2</sub> (a), H<sub>2</sub>+CO<sub>2</sub> (b). EDS Elements mapping and profiles are reported as well.

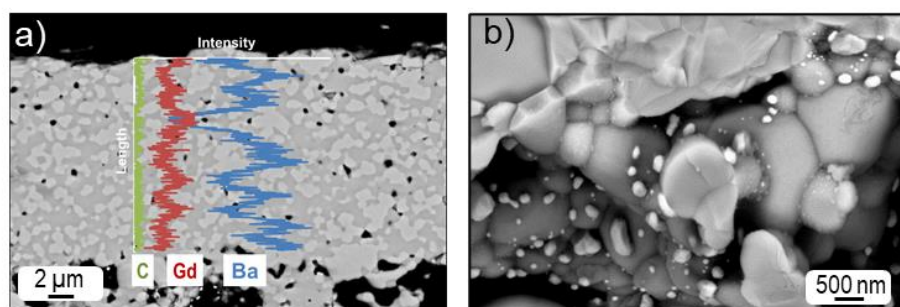


**Figure S4.** SEM micrographs of the asymmetric BCZY-GDC asymmetric membrane after permeation measurements: a) polished cross section with Ba/Gd/C EDS profiles along the dense layer thickness, b) fracture surface of Pt-infiltrated porous support at higher magnification.